Electrostatic Properties of Water at Interfaces with Nanoscale Solutes

by

Allan Dwayne Friesen

A Dissertation Presented in Partial Fulfillment
of the Requirement for the Degree
Doctor of Philosophy

Approved July 2012 by the
Graduate Supervisory Committee:

Dmitry V Matyushov, Co-Chair
C Austen Angell, Co-Chair
Oliver Beckstein
Vladimiro Mujica

ARIZONA STATE UNIVERSITY

August 2012

ABSTRACT

Molecular dynamics simulations were used to study properties of water at the interface with nanometer-size solutes. We simulated non-polar attractive Kihara cavities given by a Lennard-Jones potential shifted by a core radius. The dipolar response of the hydration layer to a uniform electric field substantially exceeds that of the bulk. For strongly attractive solutes, the collective dynamics of the hydration layer become slow compared to bulk water, as the solute size is increased. The statistics of electric field fluctuations at the solute center are Gaussian and tend toward the dielectric continuum limit with increasing solute size. A dipolar probe placed at the center of the solute is sensitive neither to the polarity excess nor to the slowed dynamics of the hydration layer.

A point dipole was introduced close to the solute-water interface to further study the statistics of electric field fluctuations generated by the water. For small dipole magnitudes, the free energy surface is single-welled, with approximately Gaussian statistics. When the dipole is increased, the free energy surface becomes double-welled, before landing in an excited state, characterized again by a single-welled surface. The intermediate region is fairly broad and is characterized by electrostatic fluctuations significantly in excess of the prediction of linear response.

We simulated a solute having the geometry of C_{180} fullerene, with dipoles introduced on each carbon. For small dipole moments, the solvent response follows the results seen for a single dipole; but for larger dipole magnitudes, the fluctuations of the solute-solvent energy pass through a second maximum. The juxtaposition of the two transitions leads to an approximately cubic scaling of the chemical potential with the dipole strengh.

Umbrella sampling techniques were used to generate free energy surfaces of the electric potential fluctuations at the heme iron in Cytochrome B562. The results were unfortunately inconclusive, as the ionic background was not effectively represented in the finite-size system.

To Darcy

TABLE OF CONTENTS

Page

LIST OF TABLES vii

LIST OF FIGURES viii

CHAPTER

1 INTRODUCTION 1

I Electrostatic solvation 3

A Solvation within linear response 3

B The solvent as a continuum dielectric 7

C Success and limitations of continuum electrostatics for modeling hydration 7

D The importance of electrostatic solvation for spectroscopy 9

II Polarization of dielectrics 11

III Properties of Water at Interfaces 17

IV Aspects of the Marcus theory of electron transfer 21

A Marcus theory 21

B Beyond Marcus theory in biological systems . . . 24

2 POLARITY PROFILE OF WATER AT THE INTERFACE WITH NON-POLAR SOLUTES 28

I Introduction 28

II Structure of the interface 30

III Polarity profile 34

IV Dynamics of the hydration layer 38

V Electrostatic solvation of dipoles 42

VI Discussion 44

CHAPTER Page

3 NON-GAUSSIAN STATISTICS OF ELECTRIC FIELD FLUCTUATIONS AT THE SOLUTE-WATER INTERFACE 46
I Introduction 46
II System 49
III Three-state model 51
IV Results 55
V Discussion 63
4 COOPERATIVE TRANSITION IN INTERFACIAL WATER . 67
I Introduction 67
II Results 68
III Chemical Potential 73
IV Discussion 76
5 FREE ENERGY SURFACE OF ELECTRIC POTENTIAL FLUCTUATIONS AT THE REDOX SITE OF CYTOCHROME B562 BY UMBRELLA SAMPLING 78
I Introduction 78
II Results 79
III Discussion 84
6 CONCLUSION 86
REFERENCES 89

APPENDIX

A SIMULATION PROTOCOL FOR NON-POLAR KIHARA CAVITIES 95
B SIMULATION PROTOCOL FOR KIHARA CAVITY WITH DIPOLE 98
C THREE-STATE PHENOMENOLOGICAL MODEL 100

CHAPTER Page

D BOUNDARY VALUE PROBLEM FOR AN OFF-CENTER DIPOLE INSIDE A SPHERICAL CAVITY IN A DIELECTRIC 103

E SOLID ANGLE 108

F DIPOLAR RESPONSE OF A SUBVOLUME 110

G SIMULATION PROTOCOL FOR FULLERENE 113

H SIMULATION PROTOCOL FOR CYTOCHROME B562 . . . 115

LIST OF TABLES

Table Page

3.1 List of model parameters produced by fitting the three-state model to $\sigma_R^2(m_0)$ from MD simulations. 55

5.1 Variance of the electric potential at the heme iron for the series of charge perturbations, δq. The quantities are normalized to the variance at $\delta q = 0$. 82

5.2 Variance of the electric potential at heme iron, due to all sources (λ^{var}), water (λ_w^{var}), protein (λ_p^{var}), and ions (λ_I^{var}), shown for $\delta q = 0$ (RED) and $\delta q = 1$ (OX). 84

5.3 Contributions to the total Stokes shift from various components of the system. The subscripts w, p and I refer respectively to the contributions from water, protein and ions. 84

A.1 Number of hydration waters used in simulations of non-polar Kihara cavities. 96

LIST OF FIGURES

Figure Page

1.1 Marcus parabolas. 22

2.1 Illustration of the Kihara solute-solvent potential. A Lennard-Jones shell is added to the surface of a hard sphere of radius r_{HS}. 29

2.2 Contact values of the solute-solvent pair distribution function. 32

2.3 The first- and second-order orientational order parameters $p^I_{1,2}$ of first-shell SPC/E water vs $r_{0\mathrm{s}} = r_{\mathrm{HS}} + \sigma_{0\mathrm{s}}$. 34

2.4 Dielectric constant of the hydration layer $\Delta\epsilon(r)$ relative to the dielectric constant of the same layer around a virtual (Lorentz) cavity. 36

2.5 Dielectric susceptibility $4\pi\chi(r)(\rho/\bar{\rho}(r))$ vs the distance r from the solute center scaled with the water diameter σ_s. 37

2.6 Exponential relaxation time of $\chi^I(t)$ (filled diamonds), $C_E(r,t)$ (open circles), and $\chi(r,t)$ (open squares). 39

2.7 Chemical potential $\mu^*_d = -\mu_d r^3_{0s}/(m_0)^2$ of solvating the point dipole m_0 at the center of the solute of radius r_{0s}. 43

3.1 Sketch of the standard expectation (a) and the picture proposed in this study (b) for the free energy of creating field R at a point within the solute when no dipole is present (equation 3.1). . . 48

3.2 Cartoon of the solute-solvent configuration. The point dipole m_0 is placed at the distance r_d from the solute center. 50

3.3 Reaction field R_0 (in V/Å) vs solute dipole m_0. 51

3.4 Illustration of the phenomenological model we use to understand our results. The surface $F(R)$ is a superposition of a ground state and two excited states. 53

3.5 Second [p_2^I, Eq. (3.8)] (main panel) and first [p_1^I, Eq. (3.7)] (inset) orientational order parameters for RD9 (r_d = 9 Å, filled squares) and RD10 (r_d = 10 Å, open squares) configurations. 54

3.6 Free energies $\mathcal{F}(m_0, R)$ (equation 3.3) for the RD10 state (r_d = 10 Å) at m_0 values indicated in the plots. 57

3.7 The average and variance of the reduced field R^* as defined by equation (3.11). 58

3.8 Comparison of results with the predictions of linear response and of continuum electrostatics. 60

3.9 Solute-oxygen pair correlation function inside the solid angle. . 61

3.10 Distributions of O-H-O angles. 63

4.1 Average (A) and variance (B) of the reduced solute-solvent, electrostatic energy u_{0s}^*. 70

4.2 Non-Gaussian parameter $\chi_G = -\beta\langle(\delta u_{0s})^2\rangle/\langle u_{0s}\rangle$. 70

4.3 First and second orientational order parameters,p_1^I and p_2^I for the first shell waters. The open circles and open squares represent, respectively the first and second parameters. 71

4.4 Exponential relaxation time, τ_2, of the slow component of the relaxation of the orientational parameter p_1^I (solid squares) and of the electrostatic solute-solvent energy u_{0s} (open circles). . . 73

Figure Page

4.5 Number of waters with oxygen within 8.5 Å of the solute center of mass. The number increases as the system goes through the crossover, then levels off as the excited state is saturated. . . . 73

4.6 Electrostatic chemical potential of the C_{180} solute calculated from thermodynamic integration. 75

5.1 Free energy surfaces, $F(\phi)$ for the RED ($\delta q = 0$) and OX ($\delta q = 1.0$) states. 80

5.2 Free energy surfaces $F(\phi)$ for different values of δq. 81

5.3 Distribution of the electric potential at the heme iron for the RED state ($\delta q = 0$). 83

5.4 Distribution of the electric potential at the heme iron for the OX state ($\delta q = 1$). 83

E.1 Illustration of the solid angle inside which the distributions were calculated. The solid angle includes all first shell waters within an arc length of $2\sigma_s$ of the dipole axis. 109

Chapter 1

INTRODUCTION

Water has long been recognized as important because of its abundance, its unusual physical properties, and its versatility as a solvent. And while water is also appreciated as critical to the environment in which all biology takes place, water is increasingly recognized as a critical active participant in biological processes at the molecular level[1]. In the area of protein folding, water release is understood to provide an entropic driving force for folding[2]. And while the hydrophobic effect is understood to lead to the burying of the protein core, water also can act as a bridge to form contacts between hydrophilic portions of the protein[1]. Water has been recognized as critical in determining the conformational dynamics of proteins[3], and in enzyme function. It can be critical for structure formation and also for the chemistry, acting as a proton donor or acceptor[1]. In bioenergetics, water is critical for maintaining proton gradients [4] and in providing the proper electrostatic environment for efficient charge transfer[5].

But for all its importance, water is puzzling. The special nature of water is indicated to first year chemistry students when it is invoked as the "anomalous" case of a substance that expands on freezing. Water is also famous for its strangely large boiling point, the density maximum slightly above the freezing point, and the triple point close to standard conditions. Recently, the nature of supercooled water has been the subject of much debate[6]. The nature of the hydrophobic effect and its role in various physical and biological processes is currently an area of vigorous research[7, 8].

In the present work, we will focus on the properties of water at the interface with nanometer-size solutes. Our emphasis will be on the electrostatic properties of water in such a situation. These properties are essential for understanding the hydration of solutes with a surface charge distribution, such as proteins or nanoparticles.

In this chapter, we will present some fundamentals of the electrostatics of solvation within linear response and within continuum electrostatics. We will consider the applications of linear solvation for spectroscopy and for electron transfer in condensed phase. And we will also examine some key properties of water at interfaces. Once a number of properties of interfacial water have been outlined, it will come as no surprise that the simple picture of solvation breaks down for hydration of nanometer size objects.

I Electrostatic solvation

A Solvation within linear response

The process of solvating a molecule can be conceptually broken into a series of steps, each contributing to the total chemical potential of a solute. The process is commonly separated into 1) the formation of a cavity and 2) insertion of the solute into the cavity. Depending on the treatment, the third step of relaxation of the cavity after solute insertion can also be included. In other treatments, this is considered as part of the second step[9, 10].

The first of these steps is commonly called cavitation, and its contribution to the total chemical potential is understood as the reversible work required to exclude the solvent from a volume. This contribution is generally a large, positive number. The second step involves the formation of solute-solvent interactions, including both long-ranged (electrostatics) and short-ranged (hydrogen bonds and Van der Waals interactions) forces. This contribution is generally negative and of similar magnitude to the cavitation free energy. Whether the chemical potential of a solute is positive or negative depends on the degree of cancellation between these two terms[9].

In the case of hydrophobic hydration, the cavitation term is the dominating contribution to the solvation free energy. In recent years, an extensive body of work has been produced on this subject. We address some of the key results on hydrophobic solvation in Section 1.3.

In the case of hydrophilic hydration, the formation of solute-water interactions outweighs the cavity-formation work, so that the total chemical potential is negative. When one considers charge transport or spectroscopic experi-

ments, the electrostatic component of the solvation becomes most important. We focus here on this aspect of hydration.

The electrostatic contribution to solvation thermodynamics of a particle in a polar liquid can be understood in terms of the solvent response to the perturbing electric field from the solute. In the absence of a solute charge distribution (i.e., all solute multipoles zero), the polarization field in the solvent fluctuates, creating fluctuations of the electric field and the electric potential inside the solute. The probability distributions of fluctuations of the electric field and potential are then obtained by projection of the systems many degrees of freedom onto the electric field or potential in the solute. For the electric field, the distribution is[11]:

$$p_0(\mathbf{E}_s) \propto \int d\Gamma \; e^{-\beta H_0(\Gamma)} \delta_3(\mathbf{E}_s(\Gamma) - \mathbf{E}_s), \tag{1.1}$$

where $\mathbf{E}_s$ is the electric field produced inside the solute by the solvent, β is the inverse temperature, $1/k_BT$, $H_0(\mathbf{E}_s)$ is the system total Hamiltonian, and $\delta_3(...)$ is the three dimensional Dirac delta function. and for the statistics of the electric potential:

$$p_0(\phi) \propto \int d\Gamma \; e^{-\beta H_0(\Gamma)} \delta(\phi(\Gamma) - \phi). \tag{1.2}$$

The probability distributions are related to the reversible work $F(\mathbf{E}_s)$ and $F(\phi)$ required for a fluctuation of $\mathbf{E}_s$ or ϕ from their equilibrium values:

$$p_0(\mathbf{E}_s) = Q_e^{-1} e^{-\beta F(\mathbf{E}_s)}, \tag{1.3}$$

and:

$$p_0(\phi) = Q_\phi^{-1} e^{-\beta F(\phi)}, \tag{1.4}$$

where Q_e and Q_ϕ are the partition functions,

$$Q_e = \int_{-\infty}^{\infty} d^3\mathbf{E}_s \; e^{-\beta F(\mathbf{E}_s)} \tag{1.5}$$

and

$$Q_\phi = \int_{-\infty}^{\infty} d\phi \; e^{-\beta F(\phi)}. \tag{1.6}$$

If a multipole is placed on the solute, the statistics of the fluctuations are modified by the electrostatic solute-solvent interaction. For a point charge q,

$$p(\phi) \propto e^{-\beta u_{0s}(\phi)} \times p_0(\phi), \tag{1.7}$$

and for a point dipole $\mathbf{m}$,

$$p(\mathbf{E}_s) \propto e^{-\beta u_{0s}(\mathbf{E}_s)} \times p_0(\mathbf{E}_s). \tag{1.8}$$

In equations 1.8 and 1.9, u_{0s} represents the solute-solvent electrostatic energy. In the case of the charge q, we have $u_{0s}(\phi) = q\phi$; for dipole solvation, $u_{0s}(\mathbf{E}_s) = -\mathbf{m} \cdot \mathbf{E}_s$.

In the case of linear solvation, the distributions $p_0(\phi)$ and $p_0(\mathbf{E}_s)$ are Gaussian, with the width of the fluctuation spectrum determined by the response function κ_i,where $i = q$ or $i = m$ indicates the response to a charge or dipole, respectively[12]:

$$p_0(\phi) \propto \exp(-\beta\phi^2/2\kappa_q) \tag{1.9}$$

and

$$p_0(\mathbf{E}_s) \propto \exp(-\beta E^2/2\kappa_m). \tag{1.10}$$

The variances are:

$$\langle(\delta\phi)^2\rangle = \kappa_q/\beta \tag{1.11}$$

and

$$\langle(\delta\mathbf{E}_s)^2\rangle = 3\kappa_m/\beta. \tag{1.12}$$

If the fluctuations are Gaussian, the effect of the multipole is simply to shift the distribution by the amount $-\kappa_q q$ or $\kappa_m m$. The average solute solvent energy is

then $u_{0s} = -\kappa_m m^2$ for a dipole and $u_{0s} = -\kappa_q q^2$ for a charge. Because of the connection of the response function κ_i to both the fluctuations and the average of the energy, one can relate the solute-solvent energy u_{0s} to the fluctuations of the field or of the potential with the multipole not present. For a charge,

$$\langle u_{0s} \rangle = q\langle \phi \rangle = -\beta q^2 \langle (\delta\phi)^2 \rangle_0 \tag{1.13}$$

and for a dipole,

$$\langle u_{0s} \rangle = -\langle \mathbf{m} \cdot \mathbf{E}_s \rangle = -\frac{\beta m^2}{3} \langle (\delta \mathbf{E}_s)^2 \rangle_0. \tag{1.14}$$

In equations 1.13 and 1.14 $\langle ... \rangle_0$ indicates the average taken in the ensemble with zero multipole. Deviations from Gaussian statistics can then be quantified in terms of the nonlinear parameter,

$$\chi_G = -\frac{\beta \langle (\delta u_{0s})^2 \rangle}{\langle u_{0s} \rangle}, \tag{1.15}$$

equal to 1 when the fluctuations are Gaussian. The electrostatic contribution to the solvation free energy can then be found from thermodynamic integration[13]. For a point charge, we have:

$$\mu_q = \int_0^q dq' \left\langle \frac{\partial u_{0s}}{\partial q} \right\rangle = -\int_0^q dq' \, \kappa_q q' = -\frac{\kappa_q}{2} q^2 = \langle u_{0s} \rangle / 2. \tag{1.16}$$

Similarly, for a point dipole:

$$\mu_m = -\frac{\kappa_m}{2} m^2 = \langle u_{0s} \rangle / 2. \tag{1.17}$$

In calculating the chemical potential, it is not necessary to include the contributions from solvent-solvent interaction, because the entropic and energetic contributions to the free energy from the solvent exactly cancel[14].

B The solvent as a continuum dielectric

For a spherical ion with radius r_{0s}, if the solvent is modeled as a dielectric with dielectric constant ϵ, one can calculate the electrostatic work for charging up the solute by integration of the energy density over the solvent volume [15]:

$$w = \frac{(\epsilon - 1)}{8\pi} \int_{r_{0s}}^{\infty} dr \; 4\pi r^2 E(r)^2. \tag{1.18}$$

The chemical potential for the point charge is then given by the familiar Born equation[16]:

$$\mu_q = \left(\frac{1}{\epsilon} - 1 \right) \frac{q^2}{2r_{0s}}. \tag{1.19}$$

For a spherical solute with a dipole at the center, solution of the Poisson equation with the Maxwell boundary conditions gives the solvation chemical potential as[17, 18]:

$$\mu_m = \frac{(\epsilon - 1)}{2\epsilon + 1} \frac{m^2}{r_{0s}^3}. \tag{1.20}$$

A derivation of equation 1.20 is given in Appendix D. The response function from the linear response formalism can then be related to the dielectric constant of the solvent:

$$\kappa_q = \frac{1 - \epsilon}{\epsilon r_{0s}^2} \tag{1.21}$$

and

$$\kappa_m = \frac{2(\epsilon - 1)}{2\epsilon + 1} \frac{1}{r_{0s}^3}. \tag{1.22}$$

C Success and limitations of continuum electrostatics for modeling hydration

The Born equation has been reported to work for ion solvation, provided certain corrections are applied[19]. It is found that in simulations of neutral ("empty") cavities, the potential inside the solute is positive [19, 20, 21]. As

a result, even if the solvent response to the charge in a cavity is harmonic, it is harmonic about a non-zero value of the solute charge. The consequence of this is that hydration of negative ions is more favorable than hydration of positive ions of the same size and charge magnitude. This can be traced back to the difference in hydration structure around positive and negative ions[19]. The effect has been noted in several simulation studies, and is also seen experimentally[22].

Similarly, the expected scaling is found for a dipolar sphere solvated in water, as long as the dipole is not too close to the interface (see Chapter 2)[23]. However, it has also been shown that for a hard cavity in a fluid of dipolar hard spheres, the chemical potential of a dipole placed at the center of the cavity scales much more strongly with the cavity radius than continuum models would predict[12].

It should be noted that the scaling of the solvation energy with the squared multipole is only a confirmation of linear response, since the continuum radius of the solute and the dielectric constant of the solvent also come into the picture. Estimation of the particle radius is problematic, since real solutes are not hard cavities, but soft particles. As a result, what generally happens is that the continuum radius is chosen from some sort of fitting that involves a former supposition of the applicability of continuum electrostatics[20, 24]. In simulations employing continuum electrostatics, the parameters are sensitive to the details of the forcefield[24]. Furthermore, since many studies are focused on water, it is difficult to check the predicted dependence of the hydration energy on the dielectric constant of the solvent; the dielectric constant is somewhere between about 70 and 80 for water at most temperatures of interest[25], so

that the factor $1 - 1/\epsilon$ is approximately 1. The same is true for the factor in the Onsager equation, $2(\epsilon - 1)/(2\epsilon + 1)$.

D The importance of electrostatic solvation for spectroscopy

When an optical probe absorbs a photon in the gas phase, the charge distribution and molecular geometry change, corresponding to the change of quantum state. The line shape of an electronic transition acquires a fine structure due to the transitions to the various possible vibrational states. Assuming that the electronic matrix element does not change with the nuclear coordinates, the probability of landing in a given vibrational state is determined by the Franck-Condon (FC) factor:

$$|\langle \chi_{i,a} | \chi_{f,b} \rangle|^2, \tag{1.23}$$

where $\chi_{a,i}$ is the nuclear wavefunction in electronic state i at the vibrational level a, and $\chi_{f,b}$ is the same quantity for final electronic state, f and vibrational state b. The (FC) factor then is the squared overlap integral between the two vibrational wavefunctions[26, 27]. Immediately following the transition, the nuclear coordinates are generally out of equilibrium, and the molecular geometry will rearrange, dissipating the energy λ_v.

If we consider now a chromophore in solution, the many solvent vibrational modes become important to the energetics. The probability of an electronic transition then depends on the statistical average of the FC factor over the vibrational states[27, 28]:

$$F(E_{i,f}) = \frac{1}{Q_i} \sum_{i,f} e^{-\beta E_{i,a}} |\langle \chi_{i,a} | \chi_{f,b} \rangle|^2 \delta(E_{i,f} + E_{i,a} - E_{f,b}), \tag{1.24}$$

where

$$Q_i = \sum_a e^{-\beta E_{i,a}}. \tag{1.25}$$

One gets a significant broadening of the line shape, due to the coupling of the electronic transition to the solvent modes[29, 28].

The reversible work associated with the rearrangement of the solvent nuclear coordinates in response to the change in electronic structure of the solute is called the solvent reorganization energy, λ_s. The solute is typically modeled as a spherical cavity in a dielectric solvent, with a dipole at the center. The change of electronic state then corresponds to a change in the solute dipole moment. Within this model, the solvent reorganization energy (or outer sphere reorganization energy) λ_s is related to the change in solute dipole moment $\mathbf{\Delta m_0}$, the cavity radius R_{0s}, and the dielectric constant of the solvent ϵ[30].

$$\lambda_s = \frac{(\Delta m_0)^2}{(R_{0s})^3}\left(\frac{\epsilon - 1}{2\epsilon + 1} - \frac{n^2 - 1}{2n^2 + 1}\right). \tag{1.26}$$

In equation 1.26, the squared refractive index n^2 refers to the solvent response on optical timescales. This is subtracted out, since we are concerned here with the relaxation of nuclear modes. In this model, the solvent response is harmonic, so that the reorganization energy for forward and reverse transitions is identical.

We define the vertical energy gap X, the reversible work required to change the electronic state with all nuclear modes frozen. The Stokes shift ΔX is then the difference in the energy gap between forward and reverse transitions. Within linear response, conservation of energy requires:

$$\Delta X = 2(\lambda_s + \lambda_v) = 2\lambda. \tag{1.27}$$

The relation of the energy gap to the Stokes shift will be addressed in more detail in the discussion of electron transfer in section IV.

Within linear response, the solvent response to changing dipole moment is also related to the fluctuations of the electric field at the solute, within one

electronic state. The solvent contribution to the linewidth is then related to the solvent reorganization energy[28]. Neglecting the vibrational contribution,

$$\frac{\beta}{2}\langle(\delta X)^2\rangle = \frac{\Delta X}{2} = \lambda_s. \tag{1.28}$$

II Polarization of dielectrics

We present here a brief discussion of polarization in dielectrics. In macroscopic electrodynamics, the medium is treated as a continuum, with molecular details coarse-grained. Rather than treating the highly heterogeneous microscopic electric field, for example, we work with the average field **E**, commonly called the Maxwell field[31]. The polarization field is handled similarly. The line of reasoning followed here is abstracted from the arguments found in the treatments by Landau[31], Fröhlich[15] and Böttcher[18].

We begin with the postulate that the electric field flux through any closed surface is equal to the charge enclosed in that surface (Gauss's law):

$$\oint d\mathbf{s}\ \mathbf{E} = 4\pi e, \tag{1.29}$$

where e is the enclosed charge, and the integral is taken over the whole surface. In differential form, equation 1.29 can be written as:

$$\text{div}\ \mathbf{E} = 4\pi\rho, \tag{1.30}$$

where ρ is the charge density. The electric field **E** is also assumed to be the gradient of a scalar potential field ϕ, satisfying the condition,

$$\text{curl}\ \mathbf{E} = 0. \tag{1.31}$$

With these assumptions, we can now write,

$$\mathbf{E} = -\text{grad}\ \phi. \tag{1.32}$$

So we recognize the electric field as the gradient of the electric potential.

Consider a conducting body placed in a uniform electric field, $\mathbf{E}_0$. The charge distribution on the conductor will arrange so that at all points on the conductor, the electric field $\mathbf{E}$ is zero. The argument for this is simple: a non-zero electric field will generate a force on any charge in the medium. Since charges in conductors are free to flow, the charge will move until the net force on the charge is zero. Furthermore, since any charge inside the body is itself a source of field, the entire charge distribution must go to the surface[31]. The result is a surface charge density σ (charge per unit surface area) given by:

$$4\pi\sigma = E_{0,n}, \tag{1.33}$$

where $E_{0,n} = \mathbf{E_0} \cdot \hat{\mathbf{n}}$ is the the projection of the electric field on the surface normal.

If one considers a dielectric instead of a conductor, the situation is different. In a dielectric, charges are bound, so that the body cannot carry a current. However, the dielectric will polarize in the presence of an external field. This is quantified by the polarization field $\mathbf{P}$, equal to the dipole moment per unit volume. The polarization field contributes a charge density $-\text{div}\ \mathbf{P} = \rho$.[1] It is instructive to consider the case of a planar interface of the dielectric with the vacuum, in a uniform external field oriented along the surface normal. A uniform polarization is induced in the dielectric, so that at all points inside the dielectric, $\text{div}\ \mathbf{P} = 0$. However, at the boundary, the polarization of the dielectric creates an apparent surface charge density, equal to the normal

[1] In a rigorous treatment, the polarization field is typically first defined as the vector field with divergence equal to the charge density: $-\text{div}\ \mathbf{P} = \rho$. It is only after the observation that integration of $-\mathbf{r}\ \text{div}\ \mathbf{P}$ over space produces the macroscopic dipole moment that we are compelled to identify the polarization field with the dipole moment per unit volume[31].

component of the surface polarization, $P_n = \mathbf{P} \cdot \hat{\mathbf{n}}$:

$$\sigma = P_n. \tag{1.34}$$

The apparent surface charge contributes an amount to the total electric field in the dielectric equal to:

$$\Delta\mathbf{E} = -4\pi\sigma\ \hat{\mathbf{n}} = -4\pi\mathbf{P}. \tag{1.35}$$

The consequence of this is that the electric field is partially screened by the polarization of the dielectric. For modest external fields, the field inside the body is reduced compared to the vacuum field by the proportionality factor $1/\epsilon$:

$$\mathbf{E} = \frac{1}{\epsilon}\mathbf{E}_0. \tag{1.36}$$

The associated difference in electric field across the interface is then:

$$\Delta\mathbf{E} = \left(\frac{1}{\epsilon} - 1\right)\mathbf{E}_0. \tag{1.37}$$

In the linear regime, the polarization in the dielectric is proportional to the electric field. Introducing the dielectric susceptibility, χ we have:

$$\mathbf{P} = \chi\mathbf{E}. \tag{1.38}$$

Comparison of equations 1.35, 1.37 and 1.38, gives the relation of the dielectric susceptibility to the dielectric constant, $\chi = (\epsilon - 1)/4\pi$, and we find:

$$\mathbf{P} = \frac{\epsilon - 1}{4\pi}\mathbf{E}. \tag{1.39}$$

Because the electric field inside a dielectric is screened by the polarization, it is useful to consider the vector field $\mathbf{D}$, called the electric displacement, that reflects only the field due to free (or "true") charges:

$$\mathbf{D} = \mathbf{E} + 4\pi\mathbf{P}. \tag{1.40}$$

In the linear regime, we have the simple relationship, $\mathbf{D} = \epsilon\mathbf{E}$. Under this circumstance, Gauss's law for free charges becomes:

$$\text{div } \mathbf{D} = 4\pi\rho_f, \tag{1.41}$$

Combining equations 1.41 and 1.32, we obtain Poisson's equation for a linear, homogeneous dielectric:

$$\epsilon\Delta\phi = 4\pi\rho_f. \tag{1.42}$$

At the boundary between two regions of space with differing dielectric constant, one applies the boundary conditions requiring the continuity of the potential ϕ and the discontinuity of the normal component of the electric field:

$$\phi_1 = \phi_2 \tag{1.43}$$

and

$$\epsilon_1 \frac{\partial\phi_1}{\partial r} = \epsilon_2 \frac{\partial\phi_2}{\partial r}. \tag{1.44}$$

Moving from a continuum description to a statistical mechanical picture, we now consider the fluctuations of the total dipole moment $\mathbf{M} = \int dV\ \mathbf{P}$ of a dielectric. For simplicity, we take any external field to be along the z direction: $E_0 = \mathbf{E_0} \cdot \hat{\mathbf{z}} = |\mathbf{E_0}|$. We focus on the statistics of the z projection of the dipole moment $M = \mathbf{M} \cdot \hat{\mathbf{z}}$. In the absence of an applied field, the statistics of the fluctuations will be given by the distribution:

$$p_0(M) \propto \int d\Gamma\ e^{-\beta H_0(\Gamma)} \delta(M(\Gamma) - M), \tag{1.45}$$

where $H_0(\Gamma)$ is the total Hamiltonian of the system at point Γ in phase space, in the absence of an applied field. The introduction of the external field modifies the system Hamiltonian to:

$$H(\Gamma, E_0) = -ME_0 + H_0(\Gamma). \tag{1.46}$$

Correspondingly, the distribution of dipoles becomes:

$$p(M) \propto e^{\beta M E_0} p_0(M). \tag{1.47}$$

The average dipole of the material is given by the statistical average,

$$\langle M \rangle = Q^{-1} \int d\Gamma \; e^{\beta M E_0 - \beta H_0(\Gamma)} M, \tag{1.48}$$

where

$$Q = \int d\Gamma \; e^{-\beta H(\Gamma, E_0)}. \tag{1.49}$$

Differentiating, we obtain (see Appendix G for details):

$$\frac{\partial \langle M \rangle}{\partial E_0} = \frac{\beta}{V} \langle (\delta M)^2 \rangle. \tag{1.50}$$

Including fluctuations of the x and y components of the system dipole, we get:

$$\frac{\partial \langle M \rangle}{\partial E_0} = \frac{\beta}{3V} \langle (\delta \mathbf{M})^2 \rangle. \tag{1.51}$$

The dielectric constant is then given by (see equation 1.39) [18]:

$$\frac{\epsilon - 1}{4\pi} = \frac{\beta}{3V} \langle (\delta \mathbf{M})^2 \rangle \times \frac{\partial E_0}{\partial E}. \tag{1.52}$$

To determine the dielectric constant, it is necessary to work out how the external field $\mathbf{E}_0$ is related to the Maxwell field $\mathbf{E}$. This is a non-trivial problem.

One can consider a spherical cavity carved from a dielectric, in an external field, $\mathbf{E}_0$. Solution of the Poisson equation with the standard boundary conditions yields the cavity field,

$$\mathbf{E}_c = \frac{3\epsilon}{2\epsilon + 1} \mathbf{E}, \tag{1.53}$$

so that the external field is reduced by the factor, $3/(2\epsilon + 1)$. If one now inserts the dielectric back into the cavity, one can calculate the electric field

generated inside the sphere due to the polarization of the surroundings by the charge distribution in the sphere. This field is called the reaction field and was first calculated by Onsager[17]:

$$\mathbf{R}_0 = \frac{2(\epsilon - 1)}{2\epsilon + 1}\frac{\mathbf{M}_s}{a^3}, \tag{1.54}$$

where $\mathbf{M}_s$ is the total dipole moment in the spherical region and a is the radius of the spherical region. If the polarization inside the sphere is given by $\mathbf{P} = (\epsilon - 1)/4\pi\mathbf{E}$, then we have:

$$\mathbf{M} = \frac{(\epsilon - 1)a^3}{3}\mathbf{E}. \tag{1.55}$$

The total field acting on the spherical region from outside sources is then the sum of the cavity field and the reaction field:

$$\mathbf{E}_e = \mathbf{E}_c + \mathbf{R}_0 = \frac{\epsilon + 1}{3}\mathbf{E}. \tag{1.56}$$

Equation 1.56 can be derived by a number of routes. We have taken the present approach to demonstrate the distinction between the total field from outside sources, $\mathbf{E}_e$ and the "directing" field[18] (the portion of $\mathbf{E}_e$ that contributes to the polarization in the subvolume). Since the reaction field orients always along the dipole moment of the subvolume under consideration, it does not contribute to the orientational statistics of the subvolume. Then for a spherical subvolume, the appropriate directing field is given by the cavity field in equation 1.53. We have for the factor in equation 1.52:

$$\frac{\partial E_0}{\partial E} = \frac{E_c}{E} = \frac{3\epsilon}{2\epsilon + 1}. \tag{1.57}$$

Using equation 1.57 in equation 1.52 we obtain Kirkwood's formula for the dielectric constant[32, 18]:

$$\frac{(\epsilon - 1)(2\epsilon + 1)}{12\pi\epsilon} = \frac{\beta N}{3V}g\mu^2, \tag{1.58}$$

where μ is the permanent dipole of a single molecule, N is the total number of molecules in the subvolume and g is called the Kirkwood factor, given by:

$$g = \frac{\langle M^2 \rangle}{N\mu^2}. \tag{1.59}$$

This equation is valid in the limit of a very large system. In practice, on the length scales used in computer simulations, and due to the boundary conditions when handling long range forces, it is necessary to apply corrections when the Kirkwood factor is calculated for finite volumes[33]. In the case of simulations performed with tinfoil boundary conditions one obtains for the dielectric constant[34, 33]:

$$\epsilon = 1 + \frac{4\pi\beta}{3V}\langle(\delta\mathbf{M})^2\rangle. \tag{1.60}$$

III Properties of Water at Interfaces

The properties of water as a solvent are determined by a combination of short-ranged hydrogen bonds and dispersion forces and long-ranged electrostatic interactions. When a nano-sized object is inserted in water, both the density profile of water and the hydrogen bond distribution are significantly altered. The orientational properties of water at interfaces are then determined by a competition between water-water hydrogen bonds and solute-solvent interactions, and therefore by the character of the solute-solvent potential, such as whether the solute is hydrophobic or hydrophilic[35, 36].

Because of water's preference for locally tetrahedral structure, the distribution of water's hydrogen bond network can be reduced to a combination of preferred orientational states at the interface [35, 37, 38]. When the interface is repulsive or only weakly attractive, the dominant configuration of interfacial waters is an ice-like structure with one unsaturated hydrogen bond pointed to-

ward the interface, along the normal; there is also a contribution from waters with their dipoles pointed in the plane of the interface[35]. The distribution of protons in this picture is essentially random, with some unsaturated H-bond donors and some H-bond acceptors pointed toward the surface.

When the solute-solvent attraction is increased, the pulling force from the surface causes a repopulation of the orientational states, causing a shift in the mean orientations, but without a significant change to the preferred orientations themselves [37]. When modest surface charges are introduced, the increased solute-solvent attraction is balanced by the increased possibility of forming hydrogen bonds in a more densely packed interface, so that the overall result is a dominantly in-plane orientation of water dipoles. The fundamental reason behind this phenomenology is the large ($\sim 4kT$) energy of hydrogen bonds in water. Because of these strong forces, the structure of the hydration shell is extremely resilient to external perturbations, which generally only cause repopulation of the different preferential surface configurations.

In contrast, for highly charged surfaces, such as at the silica-water interface, it is found that the dominant orientational state of water is actually opposite that found at hydrophobic interfaces, with the water dipoles pointed along the interface normal. This was originally found in molecular dynamics simulations, and was eventually confirmed experimentally[39, 40]. Because water is both strongly dipolar and strongly quadrupolar, the orientational properties of the interface also affect the water's electrostatic properties. This is relevant for understanding the electrostatics of hydration, both in terms of the long-range dipolar response of the solvent, as well as the fields generated from the higher multipoles of water, on shorter length scales.

In hydrophobic solvation, it has been shown that small solutes inserted into water cause little disruption to the hydrogen bond network. Consequently, the hydration free energy in such cases turns out to be controlled by the solute volume and the solvent compressibility[41, 42]. However, the hydrogen bond network is disrupted at more extensive interfaces. One therefore expects at some length scale a crossover between two types of hydrophobic hydration. Such a crossover was predicted in the Lum-Chandler-Weeks (LCW) theory of hydrophobic hydration[43]. The theory predicts that for solvation of small hard cavities in water, the hydration free energy should scale as R_{0s}^3. If the solute size is increased, at solute radii slightly larger than one solvent diameter, a crossover occurs, and the free energy of hydration then scales as R_{0s}^2. The crossover is associated with a transition from "volume dominated" to "surface dominated" hydration[12].

The LCW theory also predicts a drying of the solute-water interface for solutes larger than the crossover length scale, so that for large hydrophobes the structure of the interface is closer to the water-vapor interface[43]. In practice, what is observed around weakly attractive hydrophobic solutes in water is a "weak dewetting" of the interface[44]. In this phenomenology, the contact value of the solute-water pair correlation function first increases with solute size, for small cavities, then reaches a maximum at the point of the crossover [45, 8].

The common explanation for these observations is that a change occurs in the nature of water's hydrogen bond network near the interface, with most hydrogen bonds preserved for small solutes, and with a substantial surface disruption of the network for larger solutes[12, 39]. While this is compelling, the situation may not be so simple. It was shown that a similar crossover

occurs for hard cavities in a dipolar hard sphere fluid[12]. In this case, there are no hydrogen bonds, and the crossover might be understood in terms of a change in the orientational ordering of the dipoles at the interface. In both the case of dipolar hard spheres and hydrophobic cavities in water, the contact value of the solute-water pair correlation function reaches a maximum around the crossover, although the transition occurs at different length scales [12, 46].

The dynamics of water at microscopic length scales have been traditionally probed by Stokes-shift dynamics[47]. The dynamics of the energy gap X between ground and excited states of a chromophore is monitored. The information on relaxation is then obtained by means of the Stokes shift correlation function:

$$C(t) = \frac{\langle \delta X(t) \delta X(0) \rangle}{\langle (\delta X)^2 \rangle}. \tag{1.61}$$

The Stokes shift dynamics for free chromophores in water are found to decay on timescales faster than 1 ps. However, when chromophores are bound to proteins in solution, long tails appear, relaxing on timescales ranging from several 10s of ps[48, 49] to ns [50]. The cause of this effect has been the subject of some debate, with some claiming there is an intrinsically very slow property of hydration water seen in the Stokes shift, and with others assigning the slow dynamics to coupling of hydration waters to slow protein modes[48, 51]. The issue is clouded by the fact that the hydration dynamics cannot be separated from the complex protein dynamics. This raises the question of what is actually probed by the Stokes shift. Since dielectric models suggest that the Stokes shift probes the solvent response at very long length scales, one wonders whether Stokes shift spectroscopy is an appropriate probe for local hydration dynamics.

IV Aspects of the Marcus theory of electron transfer

A Marcus theory

By far, the most widely known and applied theory of electron transfer in condensed phase is the Marcus formalism. Marcus divides the response to a change of electronic state into two parts, called the inner and outer spheres. The inner sphere is the redox site and anything bound to it; this includes covalently bonded atoms, ligated atoms and tightly bound solvent molecules. In the case of a self exchange reaction between two ions such as Fe^{2+} and Fe^{3+}, the inner sphere would include the ion plus a first layer of hydration waters, assumed to be dielectrically saturated[52, 53]. Whatever is outside this layer constitutes the outer sphere, and is assumed to behave like a dielectric in the linear regime. Marcus observed that for such reactions the main contribution to the free energy typically comes from the outer sphere, due to the long range of electrostatic forces, and the early theory development was for reactions in which the energetics were dominated by the outer sphere, although Marcus recognized early on that this simplification was not robust[53]. The theory has since been extended to include contributions from the inner sphere. In that case, the inner sphere is assumed to comprise another harmonic contribution, uncoupled from the outer sphere[54]. Accordingly, one expects the Marcus theory not to apply to cases in which linear response fails or when the distinction between inner and outer spheres becomes unclear (for example because of binding/unbinding events, such as proton transfer)[55].

In order to formalize the electron transfer problem, an appropriate reaction coordinate must be chosen that projects the coordinates of all nuclei onto a single scalar quantity. In his original treatment, Marcus used the charge at

the redox site as a reaction coordinate. Marcus then calculated the free energy required to create the polarization that would correspond to the equilibrium polarization about the activated complex, with the electron charge divided between donor and acceptor[52, 56]. The problem was eventually put on a firmer foundation by using the vertical energy gap (energy difference between the two redox states with all nuclear coordinates frozen) as the reaction coordinate[57]. This quantity is proportional to the electric potential at the redox site, and therefore to the charge, within linear response, so that the difference between the two is purely formal. However, if the solvent response becomes nonlinear, the distinction can become more important[58]. The energy gap X as a reaction coordinate reflects the requirement of crossing the Franck-Condon barrier at $X = 0$.

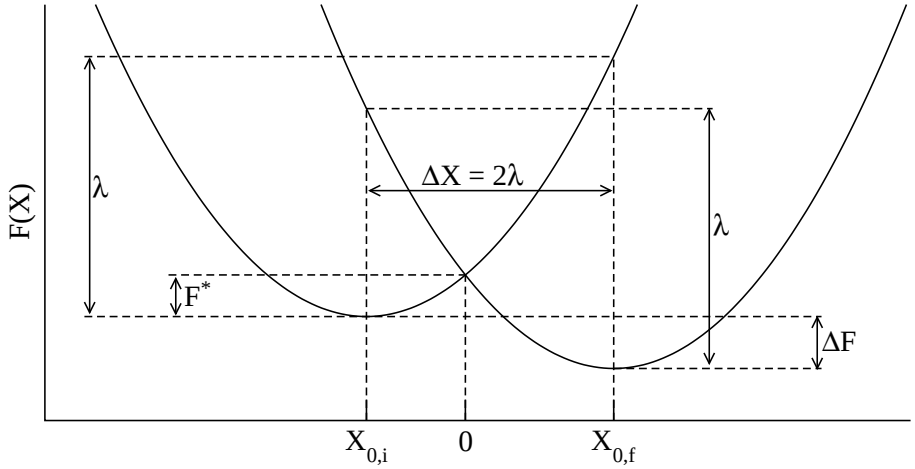

FIG. 1.1. Marcus parabolas. The parabolas are centered at minima $X_{0,i}$ and $X_{0,f}$, the equilibrium values of the energy gap in the initial (i) and final (f) states. The reorganization energy λ is dissipated in the reorganization of the nuclear coordinates following a vertical electronic transition. The activation free energy F^* is the difference in free energy between the point where the parabolas cross ($X = 0$) and the minimum free energy of the initial state, $F_i(X_{0,i})$. The difference between minima in free energy gives the activation free energy, ΔF.

Marcus treats the outer sphere response as a dielectric in the linear regime. As a result, the free energy surfaces obtained for fluctuations along the reaction coordinate are harmonic. The problem is then set up as two crossing parabolas, with the energy gap X as the reaction coordinate. In figure 1.1, the parabola on the left $F_i(X)$ represents the free energy in the initial state and $F_f(X)$ on the right represents the final state. Their minima are at $X_{0,i}$ and $X_{0,f}$, respectively. The vertical distance between the two minima is the free energy driving force for the reaction, ΔF. To understand the energetics of the electron transfer, we break the process into two steps. First, the nuclear coordinates are frozen, and the electronic state is changed from the initial state to the final state. This costs the amount of work $X_{0,i}$. Second, the nuclear coordinates are relaxed to the equilibrium point for the final electronic state; the amount of energy dissipated in this process λ_s is known as the outer shell reorganization energy or the solvent reorganization energy. The total reorganization energy λ includes contributions from the inner sphere as well. However, in the present discussion, we consider only the contribution from the solvent. The total free energy change for the sum of these two processes gives the driving force for the reaction,

$$\Delta F = X_{0,i} - \lambda_s. \tag{1.62}$$

For a radiationless electronic transition to occur, one requires that the vertical energy gap be zero. Accordingly, the transition state occurs at the point where $X = 0$, where the two parabolas cross. The free energy barrier to the reaction is then:

$$F^* = F_i(0) - F_i(X_{0,i}) = F_f(0) - F_f(X_{0,f}) + \Delta F. \tag{1.63}$$

The two parabolas in figure 1.1 must have the same curvature within linear response. Consequently, the reorganization energy is the same for forward and reverse reactions. Conservation of energy then requires that

$$-X_{0,i} - \lambda_s + X_{0,f} - \lambda_s = 0. \tag{1.64}$$

so that the Stokes shift $\Delta X = X_{0,f} - X_{0,i}$ is related to the reorganization energy. The condition of linear response further relates the Stokes shift ΔX to the variance of the energy gap. We get the relations:

$$\Delta X = 2\lambda_s = \beta\langle(\delta X)^2\rangle. \tag{1.65}$$

We will denote the reorganization energy calculated from the stokes shift as λ^{St}, and the reorganization energy from the variance, λ^{var}. The two are equal only when the statistics of the energy gap fluctuations are Gaussian. We can then evaluate the degree of non-Gaussianity in electron transfer in analogy with equation 1.15: $\chi_G = \lambda^{var}/\lambda^{St}$.

Once the relationship between λ_s and ΔX has been established, one can use simple algebra to find the point of intersection of the two parabolas. Then, for the activation free energy, we get:

$$\Delta F^* = \frac{(\lambda_s + \Delta F)^2}{4\lambda_s}. \tag{1.66}$$

B Beyond Marcus theory in biological systems

The limitations imposed by the assumption of linear response in the Marcus theory are quite stringent. The result of linear response is the connection between the reorganization energy λ_s, the free energy of reaction ΔF and the activation barrier, F^* indicated by equation 1.66. The consequence is that for a redox reaction to proceed very quickly (to have a small free energy barrier),

one must have a reorganization energy comparable in size to the driving force for the reaction. Literature calculations of the reorganization energy for redox proteins involved in photosynthesis suggest that values of λ_s are typically on the order of 0.5 eV, although measurements[59, 60] and calculations [61] produce a range of estimates ranging between 0.1 eV and 1.0 eV[62]. The energy input in photosynthesis is about 1.4 eV after which several electron hops are necessary in order to store the energy [63, 62]. In each step, free energy driving force for each of these hops is estimated to be around 0.7 eV [64]. The question arises of how the biological system has any energy left, after the several redox processes occur. These reactions are generally quite fast. Once a photon is absorbed, the initial electron transfer step happens with better than 99% efficiency. This implies a very small free energy barrier for the reaction. Thus, one expects to dissipate about half an electron volt for each hop. In this picture, the entire photon energy is lost in about three hops. It has been suggested that the reorganization energy for electron transfer in the initial events of photosynthesis was actually significantly smaller than what is usually reported from experiments [65, 66]. It was further pointed out[66] that the relevant reorganization energy for biological electron transfer might not involve all the equilibrium fluctuations of the energy gap, since these motions will be frozen on the timescale of electron transfer. This was a reasonable solution to the problem of the thermodynamics of photosynthesis, but neglected the fact that a very small reorganization energy, within the standard picture, will lead to very slow reaction rates, and that the freezing out of fluctuations eventually leads to dynamical arrest of electron transfer[67].

Eventually, work by David LeBard and Dmitry Matyushov on photosynthetic systems[62, 5, 63] showed that, in fact, when long trajectories are avail-

able, one actually calculates a reorganization energy several times *larger* than what is typically reported for experiment. Interestingly, this finding was upheld only when the reorganization energy was calculated from the variance of the potential:

$$\lambda^{var} = \frac{\beta\langle(\delta X)^2\rangle}{2}. \tag{1.67}$$

Within the linear response formalism, this is equivalent to the reorganization energy calculated from the Stokes shift:

$$\lambda^{var} = \lambda^{St} = \Delta X/2. \tag{1.68}$$

What was found, however, is that the reorganization energy from the fluctuations is several times larger than the reorganization energy from the Stokes shift. The implication is that linear response, and therefore the Marcus theory, does not apply in these systems. In the case of plastocyanin, it was found further that when the observation window was narrowed to $\sim$ 100 ps, the prediction of linear response was approximately restored. The degree of nonlinearity can be quantified through the use of the parameter χ_G, equal to 1 when fluctuations are Gaussian. This parameter was found to be of order 3 to 10 for reduction of plastocyanin and for the reactions in the bacterial photosynthesis reaction center[62, 5, 63].

The emerging picture is that biological energy chains may circumvent the limitations of the standard picture of electron transfer in two ways. First, the fluctuations of the electric potential at the redox site seem to be much larger than previously expected, and are non-Gaussian. This allows the breaking of the requirement connecting the free energy barrier to the reaction free energy. In this picture, the variance of the energy gap X is quite large, corresponding to a broad shape of the electron transfer free energy surfaces, near the minima,

leading to small activation barriers. However, the Stokes shift remains small, so that not much energy is dissipated when the electron is transferred[63].

The second point is that the large fluctuations associated with λ^{var} are associated with slow hydration dynamics. The slow component of the fluctuations does not relax on the timescale of electron transfer, so that while the large fluctuations lead to broad free energy surfaces, allowing fast electron transfer rates, very little energy is actually dissipated in the redox process [62]. The nature of the slow dynamics is not entirely clear, but it seems to be due in part to hydration water coupling to protein slow modes and in part to some intrinsically slow dynamics of water at the interface [68].

Chapter 2

POLARITY PROFILE OF WATER AT THE INTERFACE WITH NON-POLAR SOLUTES

I Introduction

To begin to address the gap between the formalism of Maxwell's continuum electrostatics and the situation for solutions of polar liquids, we used molecular dynamics simulations of model solutes to study the polarity profile of hydration shells around spherical hydrophobic solutes. Hydrophobic solvation has been the subject of extensive research in recent years, with emphasis on properties of the interface such as the density profile [46, 69], the thermodynamics of cavity formation [70] and the compressibility of hydration shells [8]. Little work has been done, however, on the electrostatic properties of hydration layers. Given the strong distortions to the density profile and the orientational structure of water at the interfaces with large solutes, in the present study, we sought to address the question of how the electrostatic properties of the hydration layer are affected.

Therefore, in contrast to existing work in this field [71, 69, 8, 46, 72], we asked the following questions: (i) how polar is the interface? (ii) how are the collective dipolar dynamics of the hydration layers affected by the solute? (iii) how are the dynamics of the hydration layer perturbed by the solute, and how far does the structural and dynamical perturbation penetrate into the solvent? (iv) are perturbations of interfacial water dynamics visible in the

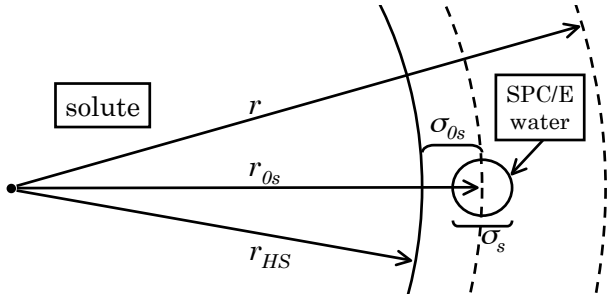

FIG. 2.1. Illustration of the Kihara solute-solvent potential. A Lennard-Jones shell is added to the surface of a hard sphere of radius $r_{\rm HS}$. The approximate position of the first peak of the solute-water pair distribution function is $r_{0s} = r_{\rm HS} + \sigma_{0s}$. The dielectric constant in Eq. (2.5) is calculated from the dipole moment of waters located between the spheres of radii r_{0s} and r shown in the graph.

Stokes-shift dynamics[47, 48]? and (v) for what solute size does the interfacial polar response approach the limit of continuum Maxwell electrostatics?

We represented the interaction between the solute and water oxygen using the Kihara potential[73, 74], which is equivalent to the Lennard-Jones potential, shifted by the core radius r_{HS}:

$$\phi_{0\rm s}(r) = 4\epsilon_{0s}\left[\left(\frac{\sigma_{0\rm s}}{r - r_{\rm HS}}\right)^{12} - \left(\frac{\sigma_{0\rm s}}{r - r_{\rm HS}}\right)^{6}\right]. \tag{2.1}$$

In this equation, σ_{0s} is the width of the solute-solvent Lennard-Jones interaction, ϵ_{0s} is the depth of the potential energy well, and r is the distance from the solute center to the water oxygen. The closest approach (first peak of the pair correlation function) of the water oxygen is then approximately $r_{0s} = r_{HS} + \sigma_{0s}$. The water-water interactions were represented by the SPC/E potential [75]. The system with these parameters is illustrated in figure 2.1.

The solute size was varied from atomic-sized to nanoscale by varying the hard radius $r_{\rm HS}$ between 0 and 12 Å. We studied systems with two different Lennard-Jones energies for the solute-solvent attraction. At the hydrophobic extreme, we studied the system with $\epsilon_{0s} = 0.65$ kcal mol^{-1}, equal to the Lennard-Jones energy of SPC/E water. Then at an opposite extreme, we stud-

ied systems with $\epsilon_{0s} = 20$ kcal/mol, comparable to the hydrogen bond energy of water.

The number of waters in the simulation box was varied to allow sufficiently thick hydration layers. For the smallest solutes, 4053 waters were included in the simulation cell, and for the largest system, 11845 water molecules were used. Systems were simulated by molecular dynamics using DLPOLY[76] at constant temperature and pressure for 5 ns, following 100 to 500 ps equilibration. A timestep of 2 fs was used and the temperature and pressure were maintained at 273 K and 0 atm using the Berendsen thermostat and barostat. Cubic periodic boundary conditions were used, and the electrostatics were handled using Ewald summation. Further simulation details are compiled in Appendix A.

II Structure of the interface

In order to understand how our model system compares to systems already in the literature, we examined the contact value of the solute-water radial distribution function and the compressibility of the first hydration shell. We defined the first hydration shell as including waters within the distance, $r \leq r_{0s} + \sigma_{0s} + \sigma_s/2$, where σ_s is the effective hard sphere diameter of water, 2.87 Å[77]. This cutoff is approximately the location of the first minimum of the solute-solvent pair correlation function.

To study the compressibility of the first hydration shell the quantity $\kappa^I = \langle(\delta N)^2\rangle/\langle N^I\rangle$ was calculated, where N^I is the number of water molecules in the first hydration shell. In the thermodynamic limit, the variance of the number of particles is related to the isothermal compressibility by $\chi_T = \beta V\langle(\delta N)^2\rangle/\langle N\rangle$ [13]. The quantity κ^I has been reported for a variety of solutes in water. The

compressibility of hydration shells has also been connected with protein denaturation. The typical result for hydrophobic solutes it that as the solute size is increased, the hydration layer becomes increasingly compressible, with κ^I passing through a minimum for solutes of modest size, with radius $\sim$3 Å. The large compressibility of hydration shells around larger solutes is associated with a "weak dewetting" transition [69], which is seen clearly from the dependence of the contact value (maximum of first peak) of the solute-solvent pair correlation function, $G_{0s}(r_{0s})$ on solute size. For large Lennard-Jones solutes[8], and for hard cavities in water[78], this function passes through a maximum, again for solutes with radius $\sim$ 3Å.

Figure 2.2 shows our results for $G_{0s}(r_{0s})$ and for κ^I, along with the data from the literature for comparison [8, 78]. In figure 2.2, the solid circles and squares represent, respectively, the Kihara solutes with small and large ϵ_{0s}. For the case of small Lennard-Jones energy, our results follow close to previous studies of hydrophobic solvation. However, for the case of the larger ϵ_{0s}, the first hydration shell has a very low compressibility, and a very large magnitude of $G_{0s}(r_{0s})$. Note also that, although there is a kink in the data around the radius of 5Å, the value of $G_{0s}(r_{0s})$ continues to increase with growing cavity radius, over the range of solute sizes studied. We also show the result for a hard cavity in a fluid of dipolar hard spheres, with reduce dipole $(m^*)^2 = \beta m^2/\sigma^3 = 1.0$.

The orientational order of water at the interface can be characterized in terms of the first- and second-order orientational parameters,

$$p_1^I = (N^I)^{-1} \langle \sum_i \hat{\mathbf{r}}_\mathbf{i} \cdot \hat{\mathbf{m}}_\mathbf{i} \rangle \tag{2.2}$$

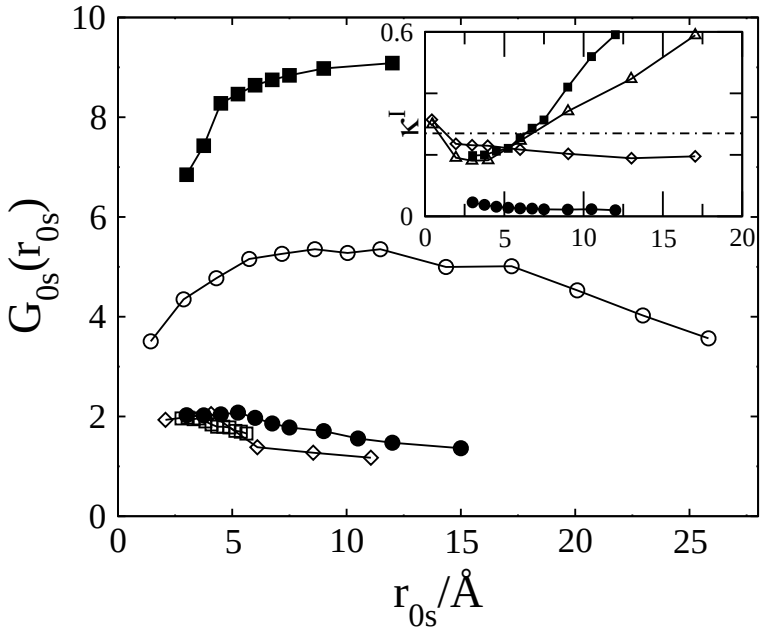

FIG. 2.2. Contact values of the solute-solvent pair distribution function. Data for the Kihara solutes with $\epsilon_{0s} = 0.65$ kJ/mol and $\epsilon_{0s} = 20$ kJ/mol are indicated, respectively, by the filled circles and filled squares. The open squares are for LJ solutes in water [45], and the open diamonds refer to hard cavities in water [46]. The case of intermediate dewetting of a hard cavity in a fluid of dipolar hard spheres with reduced dipole $(m^*)^2 = \beta m^2/\sigma_s^3 = 1.0$ [12] is shown by open circles. The inset shows first-shell compressibility $\kappa^I = \left\langle (\delta N^I)^2 \right\rangle / \left\langle N^I \right\rangle$, where N^I is the number of waters in the first shell of the solute. Results by Sarupria and Garde [8] for hard cavities in SPC/E water are shown by open triangles; open diamonds refer to data for shells in pure water, from the same work. The dash-dotted line indicates the result for bulk SPC/E water from Mittal and Hummer [78].

and

$$p_2^I = (2N^I)^{-1}\langle \sum_i 3(\hat{\mathbf{r}}_\mathbf{i} \cdot \hat{\mathbf{m}}_\mathbf{i}) - 1\rangle, \tag{2.3}$$

where $\hat{\mathbf{r}}_i$ is the unit vector from the solute center to the water center of mass and $\hat{\mathbf{m}}$ is the unit dipole vector of the ith water molecule in the first hydration shell. These parameters reflect the average cosines of the first shell water dipoles with the radial direction. We show the orientational parameters for the waters in the first hydration shell for the Kihara solute with small ϵ_{0s} (solid diamonds) and large ϵ_{0s} (solid triangles). The value of p_1^I (inset in figure 2.3) is small and positive, indicating that there is little preference of the water dipoles to orient their dipoles along or opposite to the radial direction. The value of p_2^I is however negative and significantly non-zero. The negative p_2^I reflects the tendency of waters at hydrophobic interfaces to orient in the plane of the interface. This behavior allows the interface to form with a minimal number of broken hydrogen bonds (although, of course, some strain will be introduced in the hydrogen bond network). The importance of the hydrogen bonds in the formation of the interface structure can be seen in comparison with p_2^I for dipolar hard spheres at the interface with a hard cavity from Martin and Matyushov [12] included in figure 2.3. The data are shown for reduced dipole moments $(m^*)^2$) equal to 2.0 (open squares) and 3.0 (open circles). There is a slight preference for in plan orientation, which increases for larger polarity of the solvent; however, the preference is much weaker than that for water, and in fact, p_2^I tends to even smaller values, for very large cavities. In contrast, water preserves some extent of in plane orientation, even in the limit of the planar liquid-vapor interface (single solid diamond in figure 2.3)[79].

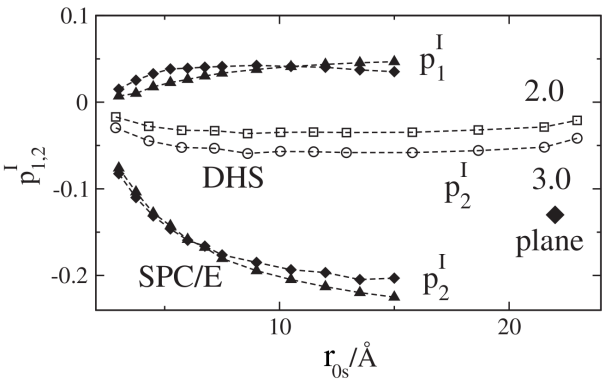

FIG. 2.3. The first- and second-order orientational order parameters $p^I_{1,2}$ of first-shell SPC/E water vs $r_{0s} = r_{HS} + \sigma_{0s}$. The solid diamonds and triangles refer to Kihara solutes in water with $\epsilon_{0s} = 0.65$ and 20 kJ/mol, respectively. The open points refer to p^I_2 for HS cavities in the fluid of dipolar hard spheres (DHS) [12] with the reduced dipole moments $(m^*)^2 = \beta m^2/\sigma_s^3$ equal to 2.0 (open squares) and 3.0 (open circles); m is the dipole moment and σ_s is the HS diameter of the solvent. The filled diamond labeled "plane" marks p^I_2 for a planar liquid-vapor interface from Ref. [79].

III Polarity profile

The polarity of a bulk liquid can be quantified in terms of the dipole induced by an external field. There are a number of options available for quantifying this response. The polarization $P(r)$ has been used in the past to define a local polarity and dielectric constant[80]. We instead consider the polarity in terms of the integrated dipole, $\mathbf{M}(r)$, equal to the total dipole moment inside the volume bounded by a sphere of radius r. In the thermodynamic limit, the susceptibility χ of the system total dipole to an external field can be calculated from the variance of the dipole moment of the sample[33]:

$$\chi = \frac{\beta}{3V}\langle(\delta\mathbf{M})^2\rangle, \tag{2.4}$$

where V is total the volume and $\mathbf{M}$ is the total dipole moment of the sample. When considering a subsystem, some researchers have extrapolated this expression for the susceptibility to small volumes. This is problematic, since the

dielectric response is normally defined in terms of the response to a uniform external field. Therefore the proper expression for the susceptibility χ_Ω of a subvolume Ω takes into account the correlation of the dipole moment in the subvolume with the total dipole of the sample[81]:

$$\chi_\Omega = (\beta/3\Omega)\langle\delta\mathbf{M}_{\mathbf{\Omega}} \cdot \delta\mathbf{M}\rangle. \tag{2.5}$$

This equation is derived in Appendix F. In order to consider the polarity of hydration layers of increasing thickness, we define the r-dependent susceptibility, $\chi(r) = (\beta/3\Omega(r))\langle\delta\mathbf{M}(r) \cdot \delta\mathbf{M}\rangle$, where $\Omega(r)$ is the volume of the hydration layer inside the distance r from the cavity center, $\mathbf{M}(r)$ is the dipole inside this volume, and $\mathbf{M}$ is the total dipole moment of the system. Because of the long-ranged nature of Coulomb interactions, calculation of the dielectric constant from simulations of finite-sized systems is non-trivial. However, in the case of simulations performed with tinfoil boundary conditions, the relationship between the dielectric constant and the dipolar fluctuations in the simulation cell is simple, with the dielectric response of the hydration layer given by: $\epsilon(r) = 1+4\pi\chi(r)$[33]. This approach naturally recovers the bulk dielectric constant for $r \to \infty$. In order to compare the polarity of the hydration layer to the polarity of bulk water, we introduce the function $\Delta\epsilon(r) = 4\pi(\chi(r) - \chi_{virt}(r))$, where $\chi_{virt}(r)$ is the susceptibility of a spherical shell having the same volume as the hydration layer, but taken from configurations of pure water. Figure 2.4 shows the polarity profile for the solutes with r_{0s} equal to 3, 7.5 and 12 Å. The excess dielectric response $\Delta\epsilon(r)$ shows a sharp peak at the interface that decays over a length of about two or three hydration shells, indicating a higher polarity close to the interface, compared with the bulk. In the case of the hydrophobic solute, the strength of the peak lessens as the solute size is

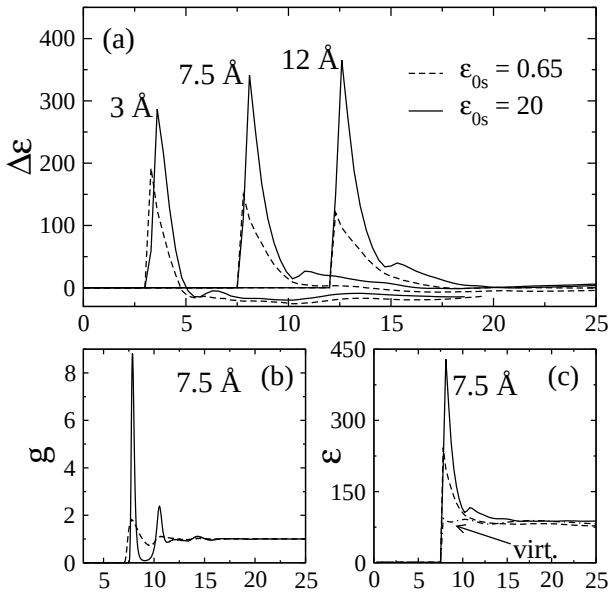

FIG. 2.4. Panel (a): Dielectric constant of the hydration layer $\Delta\epsilon(r)$ relative to the dielectric constant of the same layer around a virtual (Lorentz) cavity for three solute sizes indicated in the plot. Panel (b): Solute-oxygen pair distribution function $g_{0s}(r)$. Panel (c): Dielectric constant $\epsilon(r)$ for the Kihara solute (solid and dashed lines) and for the virtual cavity (marked as "virt.", dash-dotted line). The sizes of Kihara solutes r_{0s} are shown in the plot; the solid and dashed lines refer to $\epsilon_{0s} = 20$ and 0.65 kJ/mol, respectively. The horizontal axes in all panels refer to the distance r from the solute center (Å).

increased, but in the case of the solute with large ϵ_{0s}, the height of the peak actually increases with increasing solute size.

The susceptibility of the hydration layers was found to scale with the average density of the water layer, $\bar{\rho}(r) = N(r)/\Omega(r)$. One can consider the susceptibility per molecule, rather than per unit volume: $\chi_N(r) = \chi(r) \times \rho/\bar{\rho}(r)$, where ρ is the number density of water. This quantity is presented in figure 2.5 for the cavities with r_{0s} equal to 7.5 and 12 Å, for large (solid lines) and small (dashed lines) ϵ_{0s}, as well as for the virtual cavities of the same radius. Most of the effect of the interface is normalized out by the number of waters. This suggests that the dielectric response of water around more hydrophobic solutes may actually be less than around hydrophilic solutes.

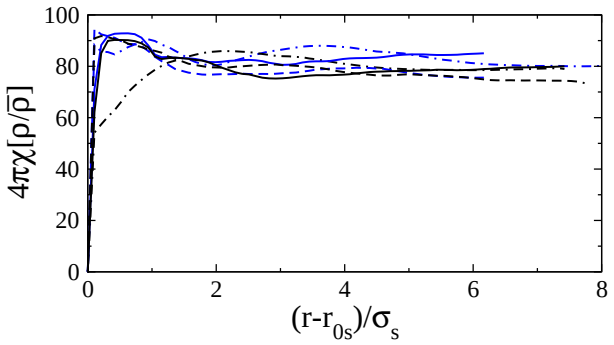

FIG. 2.5. Dielectric susceptibility $4\pi\chi(r)(\rho/\bar{\rho}(r))$ vs the distance r from the solute center scaled with the water diameter σ_s; $\bar{\rho}(r) = N(r)/\Omega(r)$ and ρ is the number density of water. Shown are the results for $r_{0s} = 12$ Å (black) and $r_{0s} = 7.5$ Å (blue), $\epsilon_{0s} = 20$ (solid lines), 0.65 (dashed lines) kJ/mol and the virtual Lorentz cavities (dash-dotted lines).

The enhanced polarization of the interface might be observable by atomic force microscopy (AFM). In the technique electric force microscopy, (EFM), a voltage is applied to the AFM tip; the resulting electric field polarizes the dielectric, and an associated additional pressure on the tip is observed.[82] For an experiment performed at constant voltage, one can calculate the electrostatic free energy as a function of the distance z between the tip and the substrate. Following the derivation of Landau[31] for the free energy due to polarizing a dielectric, we have the contribution to the free energy from polarizing the medium:

$$\Delta F(z) = \frac{1}{2}\mathbf{E}_0 \cdot \mathbf{M}, \tag{2.6}$$

where z is the distance between tip and substrate and $\mathbf{E}_0$ is the field due to external charges. The corresponding electrostatic contribution to the pressure is

$$\Delta P(z) = -z^2 \frac{\partial}{\partial z}\left(\frac{\epsilon(z)-1}{8\pi z}\right) E_0^2. \tag{2.7}$$

For large separations, z, the integrated dipole responsible for $\epsilon(z)$ will be dominated by the bulk water, and $\epsilon(z)$ is expected to be almost independent

of the distance z. However, as the tip comes close to the substrate, the regions of increased polarity near the two interfaces will begin to overlap, and the pressure is predicted to increase.

The pressure change associated with the increased dielectric response will also affect the vibration frequency of the AFM tip. This frequency is observable by the technique force modulation AFM (FM-AFM)[83]. The change in frequency is proportional to the to the gradient of the force:

$$\Delta\omega(z) \propto \frac{\partial^2}{\partial z^2}\left(\frac{\epsilon(z)-1}{8\pi z}\right)\phi^2. \tag{2.8}$$

This technique has already been used to probe the density profile near interfaces, to the level of detail that allows observation of molecular layers of surface waters [84, 85]. In the absence of an applied voltage, $\Delta\omega$ is proportional to the gradient of the water density. Consequently, discrete water layers are observed as oscillations in the tip vibration frequency. Since we observe a proportionality between the water density and the dielectric response, our work suggests that these oscillations might be significantly enhanced when a voltage is applied.

IV Dynamics of the hydration layer

Given the observation of excess polarity near the interface, it is important to ask how the dynamics of electrostatic properties are affected by the solute. As a first point, we studied the dynamics of the polarity of the hydration layer. We examined the autocorrelation function of the first-shell dipole, $\chi^I(t) = \beta\langle\delta\mathbf{M}^I(t)\cdot\delta\mathbf{M}^I(0)\rangle/(3V^I)$. We then further ask how the dynamics of the water dipole change when increasingly thick hydration layers are considered, extending the definition of $\chi^I(t)$ to $\chi(r,t)$, the time-correlation function of

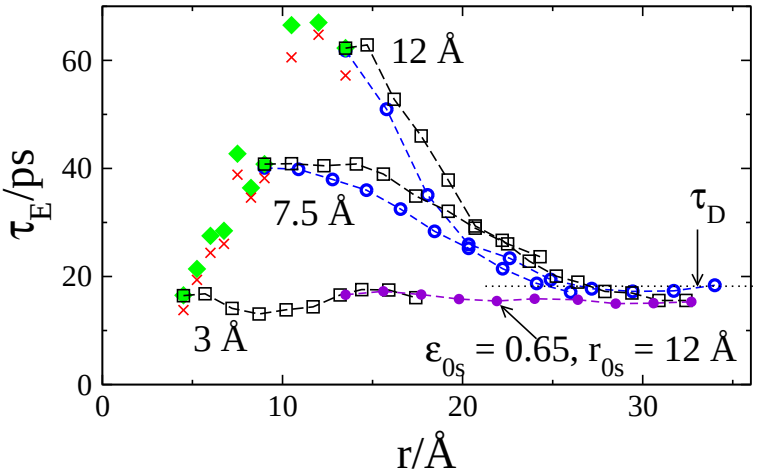

FIG. 2.6. Exponential relaxation time of $\chi^I(t)$ (filled diamonds), $C_E(r,t)$ (open circles), and $\chi(r,t)$ (open squares); $\epsilon_{0s} = 20$ kJ/mol. Also shown (crosses) is the exponential relaxation time of the self-correlation function of the unit vector $\hat{\mathbf{e}}^I(t) = \mathbf{M}^I(t)/M^I(t)$. Different solute sizes r_{0s} for the r-dependent relaxation times are indicated in the plot. The filled circles refer to $r_{0s} = 12$ Å and $\epsilon_{0s} = 0.65$ kJ/mol and the horizontal dotted line indicates the Debye relaxation time τ_D of pure SPC/E water. The dashed lines in the plot connect the points.

the water shell inside radius r. We fitted the relaxation functions to the sum of a ballistic Gaussian decay plus an exponential tail[47]. We calculated the dynamics for solutes with r_{0s} equal to 3 Å, 7.5 Å and 12 Å. Figure 2.6 presents the results for the exponential relaxation time, τ_E for the dipole moments of hydration layers of increasing thicknesses.

In the case of the larger Lennard-Jones attraction, the dynamics of the first hydration layer are significantly slowed, compared to the bulk; and furthermore, the dynamics become increasingly slow as the size of the solute increases. Interestingly, in the case of the more hydrophobic solute, this slowdown is completely absent. In order to understand the nature of the slowdown, we also calculated the relaxation time of the unit dipole in the first hydration shell (crosses in figure 2.6). The slow dynamics are controlled by the rotation of

the entire surface dipole, rather than by the motions of individual dipoles, so that the dynamics of the unit dipole follow those of the total dipole moment.

We then ask the question whether the slow dynamics of interfacial water can be probed effectively by fluorescence spectroscopy. Stokes shift spectroscopy probes the dynamics of the electric field at the chromophore. We calculated the correlation function of the electric field produced at the solute center by solvent molecules in the hydration layer, $C_E(r,t) = \langle \delta\mathbf{E}_s(r,t) \cdot \delta\mathbf{E}_s(r,0) \rangle$. These correlation functions were fit with the same form as the dipolar dynamics, and the resulting exponential relaxation times are plotted in figure 2.6 (open circles). For $r = r_1$ (only first shell waters), the slow polarization dynamics, not surprisingly, show up in the dynamics of the field at the solute center. However, because of the long-ranged nature of electrostatic interactions, as increasingly thick layers are included in the calculation, the electric field dynamics becomes insensitive to the local hydration dynamics. This underlines a key difficulty in interpreting Stokes shift correlation function data. The technique of fluorescence spectroscopy inherently probes the behavior of the solvent at a long range and is therefore not effective for elucidating the dynamics of the local hydration structure. This can be understood from the following scaling argument. The electric field from dipoles decays as r^{-3}. However, the density of solute dipoles increases as r^2. Consequently, the contribution of hydration layers to the overall electric field decreases slowly, as r^{-1}. The result is that quite distant water layers are integrated into the overall solvent response, so that the local slow dynamics are washed out. If the hydration layers are to be observed experimentally, more local techniques are needed. One such possibility is the use of a quadrupolar chromophore. The quadrupole-dipole

interaction falls off much more quickly than the dipole-dipole interaction, and would therefore probe only the closer hydration shells.

Interestingly, our results are reminiscent of Onsager's comment regarding "inverted snowball" solvation dynamics. The idea is that when a charge is solvated, the hydration structure forms far from the solute first, then "snowballs" in toward the solute, with the local structure forming last[1]. The data presented in figure 2.6 indeed support the idea that the dynamics far from the solute are faster than those near the solute. However, the results presented here are more subtle. In the case of the solute with the weaker water-solute attraction, no slowing down is observed near the interface. Additionally, the dynamical effect is strongly dependent on the solute size. Therefore, no snowball effect would be observed around a solute with weak solute-solvent attraction or around small solutes with sizes comparable to the size of our smallest studied solutes. Furthermore, even in the case of the large solutes with strong solute-solvent energy, the concept is relevant when one considers the formation of the hydration *structure*, but is no longer relevant when the solvation thermodynamics are considered, since they are dominated by the interaction of the solute with distant hydration layers. This is expected to be particularly relevant for the solvation of charges, rather than dipoles, for which the scaling of solute-solvent interactions is even more extremely weighted toward the bulk solvent.

[1] Although Onsager's comment was actually addressing the formation of the solvation structure around a solvated electron, the notion has been widely applied to solvation of ions in polar liquids[86].

V Electrostatic solvation of dipoles

In addition to the solvation dynamics, the solvation thermodynamics of a charge distribution placed inside the solute is of interest. One can consider the electrostatic chemical potential of solvation, which is the free energy of solvation of the solute charge distribution in the field from the solvent[19]. The chemical potential of a charge or dipole at the solute center is determined by the statistics of the fluctuations of the potential or the electric field at the solute, respectively. Because of the strong dependence of the electric potential on contributions from distant hydration layers, one tends to find strong system size dependence of the solvation energy and free energy of charges. We therefore focus on the fluctuations of the electric field and the solvation of dipoles.

We found that the statistics of the electric field fluctuations are Gaussian, so that the linear response approximation should be valid. Within linear response, the variance of an observable does not depend on the magnitude of the perturbation, so that one can calculate the free energy of dipole solvation from simulations of the empty solute, without the dipole actually present. In this formalism, the chemical potential of a dipole is:

$$\mu_d = -\beta(m_0)^2\langle(\delta\mathbf{E}_s)^2\rangle/6 \tag{2.9}$$

It is of interest to compare our results to the predictions of continuum electrostatics. We introduce the reduced chemical potential, $\mu_d^* = -\mu_d r_{0s}^3/(m_0)^2$; in the case of continuum electrostatics, the solvation chemical potential is given by the Onsager equation (see equation 1.20, and $\mu_d^* \simeq 0.5$, and one expects this limit to be approached for large cavity sizes. In figure 2.7, we plot μ_d^* as a function of cavity radius. The chemical potential does indeed approach

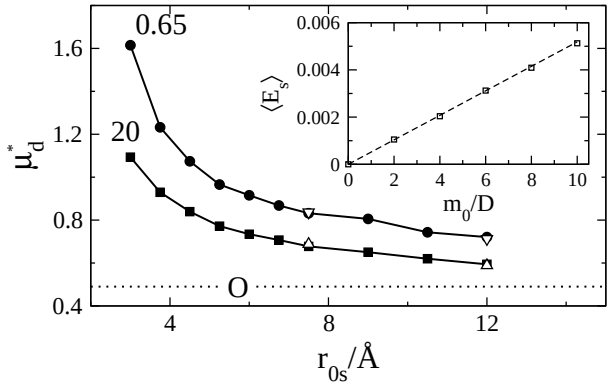

FIG. 2.7. Chemical potential $\mu_d^* = -\mu_d r_{0s}^3/(m_0)^2$ of solvating the point dipole m_0 at the center of the solute of radius r_{0s}. The solid points ($\epsilon_{0s} = 20$ kJ/mol, circles and 0.65 kJ/mol, squares) and obtained from the variance of the water electric field inside the solute with zero dipole, $\mu_d \propto \langle(\delta E_s)^2\rangle$. The open triangles are from the thermodynamic integration of the average electric field $\langle E_s \rangle$ produced by dipoles $0 < m_0 < 10$ D placed at the solute center. The average field (eV/D) is a linear function of m_0 (inset, $r_{0s} = 12$ Å, $\epsilon_{0s} = 0.65$ kJ/mol). The dashed line in the inset is the prediction based on the field variance inside the zero-dipole solute (not the best fit line); "O" indicates the Onsager equation.

the prediction of continuum electrostatics, although it is notably much higher for intermediate cavity sizes. The convergence to the continuum limit is quite slow, so that many solutes with radius less than one nanometer will fall outside the domain for which continuum electrostatics is suitable. We also find a weak dependence of the chemical potential on the solute-solvent Lennard-Jones energy. This dependence reinforces the point that one cannot effectively parameterize dielectric models of solvation on the basis of purely geometrical considerations. The nature of the solute-solvent interaction has an effect on the electrostatics of the field fluctuations in the solute, so that, while one can calculate an effective continuum cavity radius after a more rigorous calculation has been performed, continuum models of solvation are unlikely to be predictive.

To verify the effectiveness of the linear response approximation, we performed thermodynamic integration for solutes with r_{0s} equal to 7.5 Å and 12 Å. Within linear response, the electric field inside the cavity should grow linearly in response to the dipole strength in the cavity. Indeed, we find that this is the case, for dipoles up to 10 Debye. However, as will be shown later, for cases when the electric field is probed nearer the interface, linear response in fact breaks down.

Interestingly, while the strength of the Lennard-Jones energy effects the chemical potential μ_d, the effect is small, compared to the effect of changing the solute radius, r_{0s}. Because the two LJ energies used are at the extremes of intermolecular interactions, the region between the two curves in figure 2.7 may in fact define a region inside which most systems of practical interest in chemistry will fall. Deviation from this region will likely be an indication of nonlinear solvation, in which local solvent structure becomes important to the thermodynamics.

VI Discussion

Addressing the questions posed at the front of this chapter, we have found (i) a large excess polarization in the water near the solute-solvent interface. From the studies of dynamics, we find (ii) that at certain interfaces, the dipolar dynamics can become significantly slowed, compared to bulk water, and that the slower dynamics can also be seen in the electric field produced by first shell waters. Addressing the question of length scales (iii), we find that the dynamical and structural perturbations are significant for hydrations layers with thickness up to approximately 1 nm. We also find (iv) that the slowed dynamics of surface waters are not recorded by the Stokes shift dynamics of

a dipolar probe placed at the solute center. We also confirm that (v) the Onsager result for dipole solvation is approached from above, with increasing cavity radius, and that convergence to this limit is slow.

Given that the polarity scales with the water density, we are able to suggest a link between the wettability of a solute and the polarity of the hydration layer. We also note that the dependence of the water dynamics on the surface composition can lead to the existence of slow and fast domains on a heterogeneous surface[72]. However, we also point out that this sort of heterogeneity will not necessarily be picked up by Stokes shift dynamics, and there is a need for experiments that are more sensitive to the local hydration dynamics.

Chapter 3

NON-GAUSSIAN STATISTICS OF ELECTRIC FIELD FLUCTUATIONS AT THE SOLUTE-WATER INTERFACE

I Introduction

As discussed in chapter 1, the electric field produced by the solvent inside a solute is a fluctuating variable. For the case when no external field is applied, we will denote this field as $\mathbf{R}$. If this field is probed at a dipole $\mathbf{m}_0$ placed on the solute, the average value of $\mathbf{R}$ at the dipole is called the reaction field, $\mathbf{R}_0 = \langle \mathbf{R} \rangle$. In this chapter, we aim to understand the statistics of $\mathbf{R}$ produced by water at the interface with a non-polar solute. We introduce a point dipole close to the solute water interface and study the statistics of $\mathbf{R}$ as the dipole magnitude is increased. Our focus is on the projection of the field on the direction of the dipole $\hat{\mathbf{m}}_0$; accordingly, we introduce the coordinate $R = \hat{\mathbf{m}}_0 \cdot \mathbf{R}$. The reversible work required for a fluctuation of R away from its equilibrium value is described by the Landau functional[87] $F(R)$ and the associated distribution:

$$p(R) \propto e^{-\beta F(R)} \propto \int \delta\left(R - R(\Gamma)\right) e^{-\beta H_0} d\Gamma, \tag{3.1}$$

where H_0 is the total system Hamiltonian. The functional $F(R)$ represents the free energy surface of electric field fluctuations in the absence of a perturbation from the solute dipole (*i.e.*, $m_0 \to 0$). Within the linear response approximation, the statistics of R are expected to be Gaussian, and the free

energy surface is parabolic with response function κ:

$$F(R) = R^2/(2\kappa). \tag{3.2}$$

Introduction of the point dipole modifies the free energy surface to

$$\mathcal{F}(m_0, R) = -m_0 R + F(R). \tag{3.3}$$

The result, within linear response, is that the shape of the distribution $p(R)$ is not modified, but only shifted by the amount κm_0 (see chapter 1 for a more detailed discussion).

However, one can imagine that for some situations of interest the shape of $F(R)$ might be significantly non-parabolic. Consider the solvent response to an increasing solute dipole. As the field from the solute increases, frustration is built up in the water hydrogen bond network as the water dipoles align increasingly with the field. Under strong enough fields, the frustration could be released, with the water landing in a new state. This new state would be expected to be harmonic, but around a different (non-zero) minimum, R_1 (figure 3.1).

If the scenario described above were realized, several predictions could be made about the expected resulting observations. If the structure of water lands in a new state, the curvature of the free energy surface in that state would likely be different from that in the ground state. The width of thermal fluctuations about the minimum R_1 would be expected to be different from those around zero. With changing solute dipole m_0, the excited state would be expected to be reduced in free energy by the amount $-m_0 R_1$ so that states normally thermally inaccessible to water could become significantly populated. At some intermediate values of the solute dipole $m_0 \simeq F_0/R_1$, one would

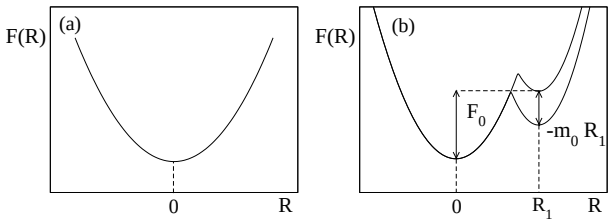

FIG. 3.1. Sketch of the standard expectation (a) and the picture proposed in this study (b) for the free energy of creating field R at a point within the solute when no dipole is present (equation 3.1). In our simulations, a point dipole is placed at that point, which modifies the free energy to $\mathcal{F}(m_0, R)$ (equation 3.3). The traditional linear-response approximation anticipates $F(R)$ to be harmonic in the whole range of R-values of interest. In contrast, we suggest the existence of an excited state, with the corresponding minimum lifted by the free energy F_0. This excited state, too high to be observed in the homogeneous liquid or in non-polar solution, can become observable by placing the dipole m_0 into the solute, which lowers the free energy gap between the lower and higher minima by $-m_0 R_1$. The curvature of the excited state near its minimum might be different from the corresponding curvature at the lower minimum, thus altering the basic assumption of the linear-response approximation, the invariance of the spectrum of the solvent fluctuations with respect to the magnitude of m_0. The overall shift of $F(R)$ in the external field is not shown in the diagram; the positions of the lower minimum at zero and nonzero dipoles m_0 are therefore made to coincide.

expect significant probabilities of finding the surface water in either state. The surface waters would then be expected to switch between states, increasing the variance of the reaction field by an amount of order $(R_1)^2$.

One particularly likely scenario for observing excited configurational states of water is at the interface with solutes of approximately nanometer size. Waters at such an interface already experience some degree of structural frustration. Hydration water around such solutes is characterized by a tendency of the waters to orient with their dipole moments in the plane of the solute-water interface. This structure helps to minimize the number of unsaturated bonds produced by opening up a cavity in the solvent. The introduction of a polar group near the interface could then induce a competition for some surface waters between this characteristic structure, and a structure in which the water

dipole is flipped to coordinate with the solute dipole. The existence of multiple orientational states of interfacial water has in fact been demonstrated already [88, 36, 35]. What has been missing to this point is a study of the ability of water to switch discontinuously between different states, and the effect of such a switching on the thermodynamics of solvation. The primary finding of the present study is the existence of such a crossover and the implications for the electrostatics of hydration.

II System

In the present work, we use molecular dynamics (MD) simulations of a nonpolar solute hydrated in SPC/E water. The interactions of the solute with water oxygen are given again by the Kihara potential:

$$\phi_{0s}(r) = 4\epsilon_{0s}\left[\left(\frac{\sigma_{0s}}{r - r_{\mathrm{HS}}}\right)^{12} - \left(\frac{\sigma_{0s}}{r - r_{\mathrm{HS}}}\right)^{6}\right]. \tag{3.4}$$

We then introduce a point dipole, oriented along the radial direction and located a distance r_d from the solute center (see figure 3.2). We study dipoles up to 10 Debye in magnitude, and situated at two distances, $r_d = 9$ Å and $r_d = 10$ Å from the solute center. Further simulation details are given in Appendix B.

We study the change in the spectrum of fluctuations of the water electric field R, measured at the solute dipole, as the solute dipole moment is increased. Figure 3.3 shows the dependence of the reaction field R on the solute dipole. The top panel in figure 3.3 shows the results for $r_d = 10$ Å, and the bottom panel shows the data for $r_d = 9$ Å. For small magnitudes of the solute dipole, the prediction of linear response is followed, and the reaction field scales with the dipole moment. But as the dipole moment is increased further, a crossover

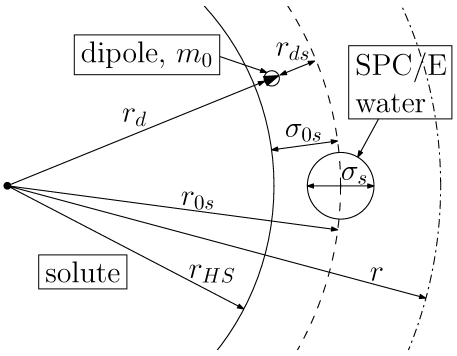

FIG. 3.2. Cartoon of the solute-solvent configuration. The solute is a hard core of radius $r_{\rm HS}$ covered with the LJ layer of the width σ_{0s} (Eq. 3.4). The distance $r_{0s} = r_{\rm HS}+\sigma_{0s}$ approximately corresponds to the first peak of the solute-solvent pair distribution function $g_{0s}(r)$ (also see Fig. 3.9 below). The point dipole m_0 is placed at the distance r_d from the solute center and, correspondingly, the distance $r_{ds} = r_{0s} - r_{\rm HS}$ from the solute-solvent interface. The solvent is SPC/E water at 1 atm and 273 K (the melting temperature of SPC/E water is 215 K[89]).

occurs. After the crossover, the reaction field again scales linearly with the solute dipole, but projects to a non-zero value for the reaction field at zero dipole, as would be expected if the system had landed in a new minimum of the free energy surface. The scaling in the intermediate region of dipole strengths is approximately quadratic. In the two linear regions, the slope of the reaction field with the dipole moment corresponds to the curvature of the free energy surface, $F(R)$. As the system lands in the new minimum (second linear region), the curvature of the Landau functional clearly changes, as can be seen in the difference in slopes between the small dipole and large dipole regions of the plots in figure 3.3. We suggest that this phenomenology is due to the appearance of a different, previously unoccupied (or very sparsely occupied) state of interfacial water molecules.

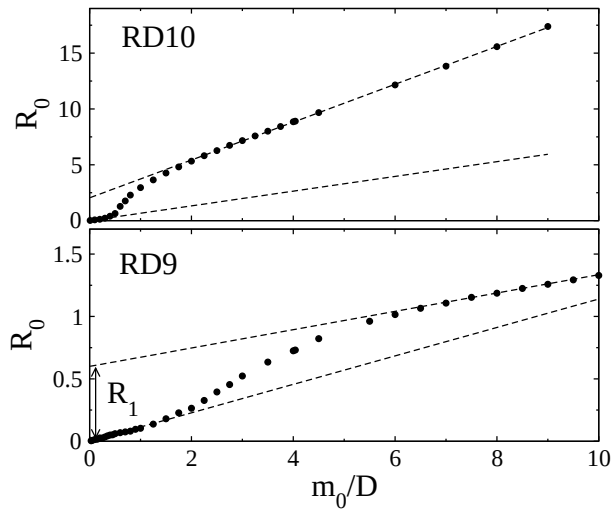

FIG. 3.3. Reaction field R_0 (in V/Å) vs solute dipole m_0 for RD9 (r_d = 9 Å) and RD10 (r_d = 10 Å) configurations (see Fig. 3.2). The dashed lines show the slopes of the linear portions of $R_0(m_0)$. The scaling of R_0 with m_0 is approximately quadratic in the intermediate region. The vertical arrow in the lower panel indicates the equilibrium field R_1 in the excited state obtained by extrapolating the reaction field in the excited configuration to zero solute dipole (Fig. 3.1).

III Three-state model

At this point, we describe the three-state phenomenological model that provides an analytical framework for understanding the detailed results of our simulations. The model assumes three harmonic states of hydration water. The ground state (g) is responsible for most of the solvent fluctuations in the absence of any perturbing field. This is the state centered at zero reaction field. In general, the reaction field is, by definition, oriented along the solute dipole moment. However, for purposes of describing the fluctuations of a stochastic variable, R, we define the positive reaction field to be along the radial direction, $\hat{\mathbf{r}}_d = \mathbf{r}_d/r_d$, rather than along the dipole direction, so that negative reaction field corresponds to the field pointed toward the solute center. We further introduce two excited states (1 and 2) centered at fields R_1 and R_2, corresponding to the positive (1) and negative (2) reaction fields. The

solvent response in each state, g, 1, 2, is characterized respectively by κ_α, with $\alpha = g$, 1, 2. The response functions κ_α have dimensions of inverse volume; we can then define the length scale, $\ell_R^\alpha = \kappa_\alpha^{-1/3}$. This length scale reflects the depth at which the a dipolar probe placed in the solute will be affected by the solvent fluctuations. We introduce three states, rather than just the two described in the introduction, in order to reflect the possibility of the surface dipoles flipping to orient either along or against the radial direction (see figure 3.4). The minima of the two states are lifted by the free energies F_1 and F_2 above the ground state.

The introduction of the solute dipole modifies the free energy surfaces in each of the three states, by lowering the free energy by the amount, $-m_0 R$. The free energies of the three states (g, 1, 2) are then given by:

$$\mathcal{F}_\alpha(m_0, R) = F_\alpha(R) - m_0 R. \tag{3.5}$$

The total free energy surface describing the reaction field fluctuations is then given by the trace over the states available to the system:

$$e^{-\beta\mathcal{F}(m_0,R)} = \sum_\alpha e^{-\beta\mathcal{F}_\alpha(m_0,R)}. \tag{3.6}$$

As with our previous simulations of Kihara solutes with no perturbing dipole, we calculated the first and second orientational parameters, p_1^I and p_2^I, of the waters in the first hydration shell:

$$p_1^I = (N^I)^{-1} \sum_{j=1,N^I} \hat{\mathbf{m}}_j \cdot \hat{\mathbf{r}}_j, \tag{3.7}$$

and

$$p_2^I = (2N^I)^{-1} \sum_{j=1,N^I} \left[3(\hat{\mathbf{m}}_j \cdot \hat{\mathbf{r}}_j)^2 - 1\right]. \tag{3.8}$$

The results for the first orientational parameter are shown in panel A of figure 3.5. The value of p_1^I is close to zero, indicating almost no asymmetry in

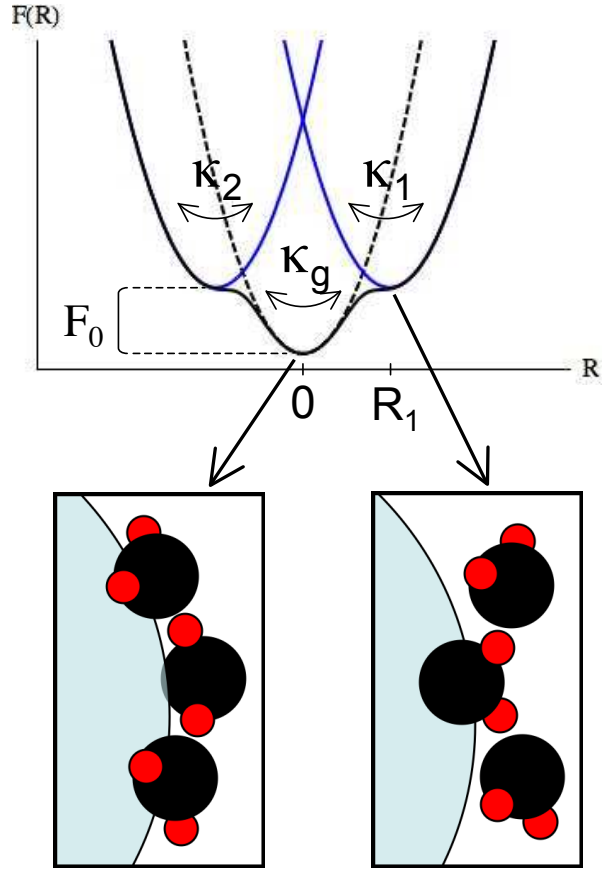

FIG. 3.4. Illustration of the phenomenological model we use to understand our results. The surface $F(R)$ is a superposition of a ground state and two excited states lifted above the ground state by the free energy F_1 (top panel). The bottom panel shows a cartoon of the two scenarios for the excited state. A water molecule breaks free from the hydrogen bond network and coordinates with the field from the solute.

the orientation of the hydration waters, corresponding to approximately zero electric field inside the cavity at zero solute dipole. The second orientational parameter, however, is significantly negative, indicating a tendency for the water dipoles to orient in the plane of the interface.

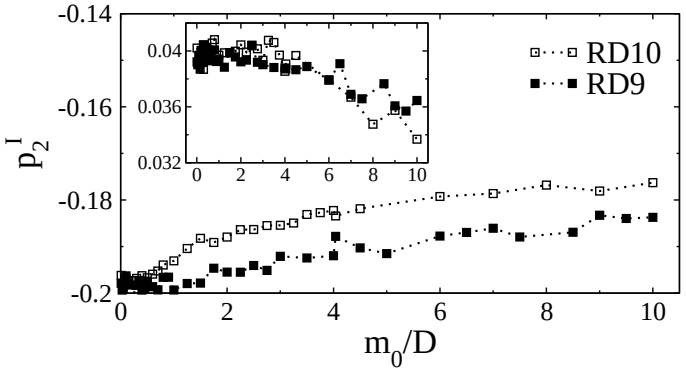

FIG. 3.5. Second [p_2^I, Eq. (3.8)] (main panel) and first [p_1^I, Eq. (3.7)] (inset) orientational order parameters for RD9 ($r_d = 9$ Å, filled squares) and RD10 ($r_d = 10$ Å, open squares) configurations.

These results, along with the observation that $\langle R \rangle \simeq 0$ when $m_0 \to 0$, indicate that there is little asymmetry in the distribution of thermally accessible configurations of the interfacial dipoles at $m_0 \to 0$, due to the low populations of the excited states. Our data for positive m_0 are not very sensitive to the values of R_2 and F_2. As a result, adequate numerical fits of the simulation data are produced with a reduced set of model parameters: $R_1 = -R_2$,

$F_1 = F_2 = F_0$ and $\kappa_1 = \kappa_2$ [1]. The free energies of the three states then become

$$\begin{aligned} F_g(R) =& R^2/(2\kappa_g), \\ F_1(R) =& (R - R_1)^2/(2\kappa_1) + F_0, \\ F_2(R) =& (R + R_1)^2/(2\kappa_1) + F_0. \end{aligned} \tag{3.9}$$

Four model parameters κ_g, κ_1, R_1, and F_0 were fitted to the field variance $\sigma_R^2(m_0)$ from MD data (see figure 3.7a). They are listed in Table 3.1 and are used to produce plots of $R_0(m_0)$, $\sigma_R^2(m_0)$, and $\mathcal{F}(m_0, R)$ presented in the Results section below.

Table 3.1. List of model parameters produced by fitting the three-state model to $\sigma_R^2(m_0)$ from MD simulations. $\ell_R^\alpha = (\kappa_\alpha)^{-1/3}$, $\alpha = \mathrm{g}, 1$ is the characteristic length of penetration of water's surface fluctuations into the solute.

Configuration	r_d, Å	βF_0	ℓ_R^g, Å	ℓ_R^1, Å	R_1, V/Å
RD9	9	7.3	3.0	3.1	0.3
RD10	10	7.2	1.5	1.2	1.0

IV Results

All the simulation results that we discuss below have been produced for two distances between the point dipole in the solute and its center (Fig. 3.2),

[1] Because of the asymmetry of water's molecular charge, the free energy surface $\mathcal{F}(0, R)$ is in principle asymmetric with respect to the transformation $R \to -R$. Excitations to the R_2 state probably require less free energy, $F_2 < F_1$, since less stringent rearrangement of the hydrogen bond network is required. This problem warrants further studies, in particular in applications to surfaces with alternating charges, such as those of proteins. Our present results, restricted to solute dipoles parallel to the radial direction $\hat{\mathbf{r}}_d$ do not show significant deviations from the assumed symmetric behavior, although fits to the model might improve if this requirement is lifted at the expense of a larger number of fitting parameters.

r_d = 9 Å and r_d = 10 Å. We will reference them below as states RD9 and RD10, respectively.

As noted above, the dependence of the reaction field R on the solute dipole m_0 is characterized by two linear regions, with a fairly broad crossover region, which is the signature of the transition between the lower (ground) and the higher free-energy states of the solvent. The two states are clearly distinguished in the changes in the free energy surfaces of reaction field fluctuations, as the solute dipole is increased. Figure 3.6 shows the free energy surfaces for the RD10 state for several solute dipoles, as the system passes through the crossover. Initially, the surface is single-welled, although it should be noted that the wings of the curve are almost flat, rather than parabolic. For slightly larger values of m_0, a shoulder appears at higher values of R. As the solute dipole is increased further, the surface becomes double-welled; at still higher dipole moments, the surface water moves completely into the excited state, and the free energy surface returns to a single-welled shape. The overall behavior is reminiscent of the phenomenology of a first order phase transition; however, it should be noted that the observations reported here seem to correspond to a fairly localized change in the solvent structure, involving just a few water molecules (see below).

The phenomenology of first order phase transitions generally predicts that far from the transition point, fluctuations will be Gaussian. As the transition point is approached, the statistics of fluctuations are expected to become significantly non-Gaussian, with a maximum in the fluctuations occurring near the transition point[90]. For example, in the case of a temperature-controlled transition, one expects a spike in the heat capacity. As expected, our results show a peak in the variance of the reaction field, $\sigma_R^2 = \langle(\delta R)^2\rangle$, when the

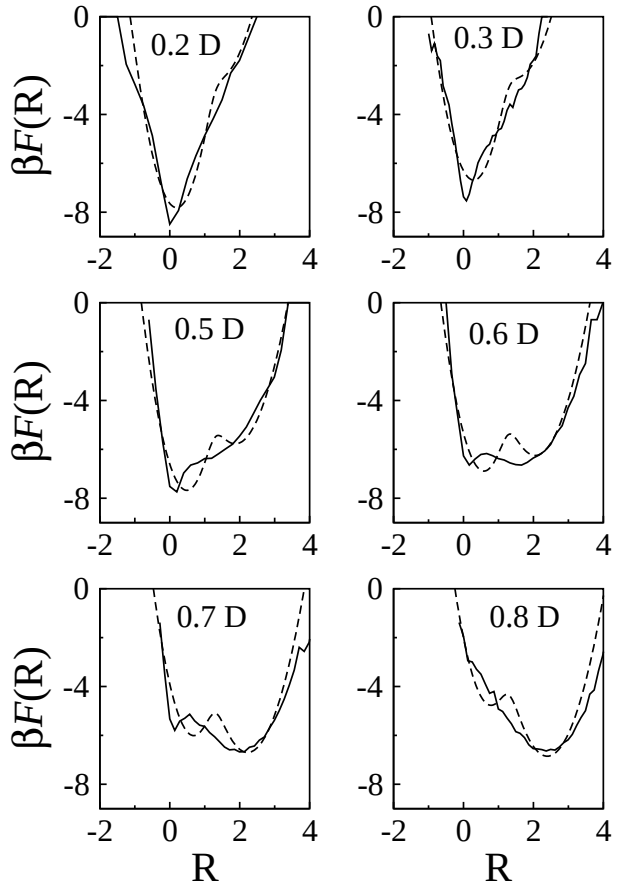

FIG. 3.6. Free energies $\mathcal{F}(m_0, R)$ (equation 3.3) for the RD10 state ($r_d = 10$ Å) at m_0 values indicated in the plots. The electric field at the solute dipole in the abscissa is in V/Å; the dashed lines refer to the fits to the three-state model (equations 3.5 and 3.6). The model parameters used in the plot are listed in Table 3.1. For reference, 1 Debye in the RD10 state corresponds to a reduced dipole $m^* = 3.0$ (see equation 3.10 below).

system passes through the transition, as shown in figure 3.7. The results are plotted against a reduced dipole moment that reflects approximately the ratio of fields produced by the solute and by neighboring water molecules at the solute-water interface:

$$m_0^* = \frac{m_0}{m_s} \left(\frac{\sigma_s}{r_{ds}} \right)^3 , \tag{3.10}$$

where m_s and σ_s are the solvent (water) dipole moment and diameter, respectively, and $r_{ds} = r_{0s} - r_{\mathrm{HS}}$ is the distance from the dipole to the solute-water

interface. Similar ideas are used to introduce the reduced instantaneous field:

$$R^* = Rr_{ds}^3/m_s. \tag{3.11}$$

Its average, R_0^*, and variance, $\langle(\delta R^*)^2\rangle$, are shown in Fig. 3.7.

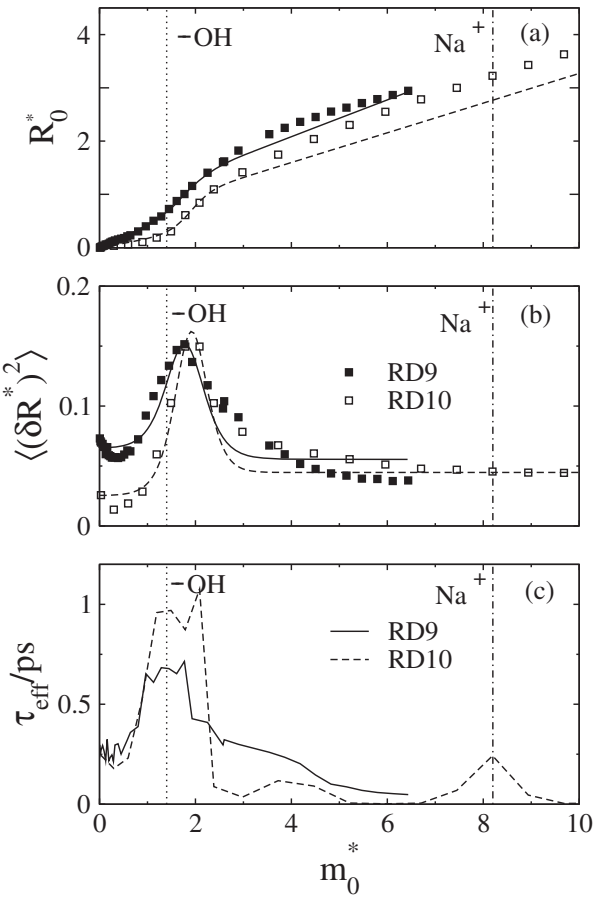

FIG. 3.7. The average, R_0^*, of the reduced field R^* as defined by Eq. (3.11) (a) and its variance (b) vs the reduced solute dipole defined by Eq. (3.10). The filled squares and solid lines in (a) and (b) refer, respectively, to the MD results and their fit to the three-state model for the RD9 configuration; the open squares and the dashed lines carry the same information for the RD10 configuration. Panel (c) shows the relaxation time τ_{eff} of the water field self-correlation function (see text) obtained from MD simulations for RD9 (solid line) and RD10 (dashed line) configurations. The dotted vertical line shows the approximate field generated by the hydroxyl of aqueous methanol at the nearest water oxygen, and the dash-dotted vertical line corresponds to the same quantity for sodium ion in water.

In order to provide context for these results, we estimated the field strengths produced by sodium ion and by the hydroxyl of aqueous methanol at the nearest water oxygen. The solute-water distances required for this estimate are taken from corresponding distribution functions from references [19] and [91]. The vertical lines in figure 3.7 are drawn at the values of m_0^* that reflect the fields from these solutes, normalized in the same way as m_0^* and R^*. The field of a hydroxyl falls in the range that is expected to produce significant populations of both water states. In contrast, the much stronger field of the sodium cation is sufficient to push the interfacial water predominantly into the excited state.

To study the dynamics associated with the crossover, we calculated the time self-correlation function, $S(t) = \langle \delta R(t) \delta R(0) \rangle / \langle (\delta R)^2 \rangle$. We fit the relaxation function to a sum of exponentials; one can then define an average relaxation time, $\tau_{\text{eff}} = \int_0^\infty dt S(t)$. This relaxation time passes through a maximum in the same range as the spike in the field variance, similar to the critical slowing associated with first order phase transitions[92, 93].

The degree of deviation from Gaussian statistics can be quantified by the parameter $\chi_G = m_0 \beta \langle (\delta R)^2 \rangle / \langle R \rangle$, the temperature-reduced ratio of the variance of the solute-water energy to its average, equal to 1 when the linear response approximation is valid. This parameter is plotted for increasing solute dipole in figure 3.8. Not surprisingly, we see a spike in this parameter in the area of the transition. In order to elucidate the extent of the deviation from linear response, we show in figure 3.6 the direct calculation of the reaction field factor, κ from the ratio of the reaction field to the solute dipole; that is, $\kappa = R_0/m_0$. We compare this to the prediction of linear response, calculated from fluctuations in the cavity: $\kappa = \beta \sigma_R^2$. Again, since in linear response

this variance is independent of the solute dipole, the horizontal dashed line in figure 3.6 reflects the value to which both these quantities converge if linear response is applicable.

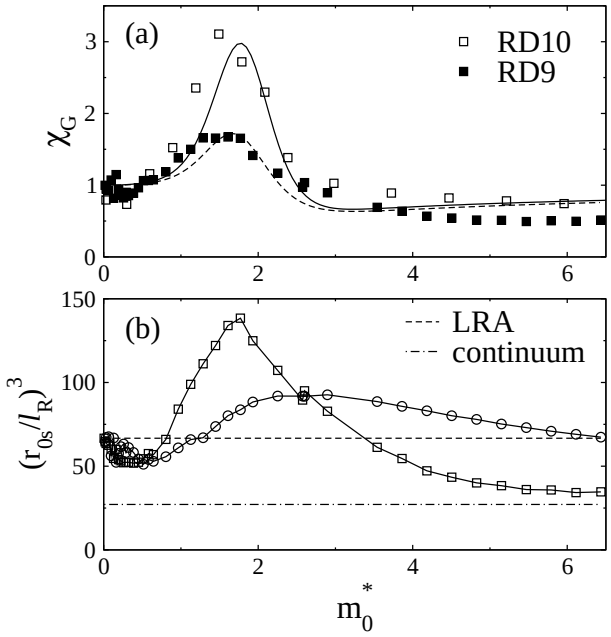

FIG. 3.8. Comparison of results with the predictions of linear response and of continuum electrostatics. In panel (a), we show the Nonlinearity parameter χ_G (equation 1.15) obtained from MD simulations (points) and from fitting the three-state model (lines). Panel (b) shows the reduced stiffness parameter $\kappa r_{0s}^3 = (r_{0s}/\ell_R)^3$ calculated in different approximations for RD9. The dash-dotted line, $\kappa = R_0/m_0$, is from the dielectric continuum calculation for the reaction field at a dipole inside a dielectric cavity (Eq. 3.12). The dashed line shows $\kappa = \beta\sigma_R^2$ obtained from the variance σ_R^2 at $m_0 = 0$. The open circles show $\kappa = R_0/m_0$ and open squares refer to $\kappa = \beta\sigma_R^2$, both from MD simulations. In linear response, circles and squares are expected to collapse on the dashed line (Eq. 1.12).

To give further context to these results, we also indicate the value obtained for κ if the solute is modeled as a point dipole placed inside a cavity ($\epsilon = 1$) in a continuum dielectric. The reaction field in this approximation is given, to a very good approximation, by:

$$R_0 = \frac{m_0}{r_{0s}^3}\frac{\epsilon - 1}{2\epsilon + 1}\left(2 - \frac{z^2}{\epsilon + 1}\right)\frac{1 + z^2}{(1 - z^2)^3}, \tag{3.12}$$

where $z = r_d/r_{0s}$. The derivation of this result is given in Appendix D. The continuum cavity radius in this calculation was chosen at $r_{0s} = 11.5$ Å, slightly below the position of the first peak of the solute-solvent pair distribution function at $\simeq 12$ Å(Fig. 3.9). This value was chosen for a number of reasons, given in Appendix D. Most importantly, however, this value for the continuum radius produces the proper scaling of the reaction field with the dipole-interface distance: $R \sim r_{0s}^{-3}$. The choice of a value that produces this scaling allowed the collapse of the data in figure 3.3; when this value is used for the continuum cavity radius, the solvent response approaches the prediction of continuum electrostatics for large dipoles.

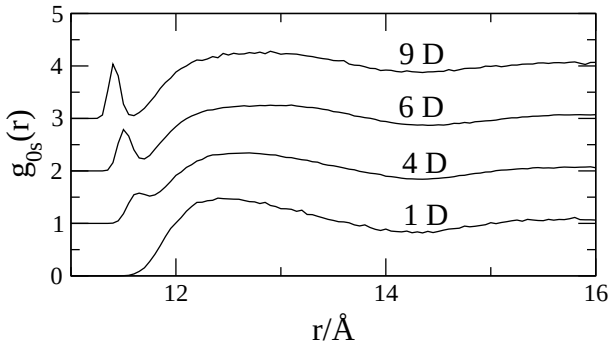

FIG. 3.9. Solute-oxygen pair correlation function for RD9, inside the solid angle defined in the text (also see Appendix E). The numbers in the plot indicate values of the dipole moment m_0. The curves are shifted vertically by 1.0 for a better view.

Having drawn the comparison of the observed phenomenology to that of phase transitions, the question naturally arises of what is the nature of the structural change associated with the excited state of the surface water. Specifically, one wonders what is the spacial extent of the structural perturbation. Our results presented above for the orientational parameters of the surface waters seem to imply that the transition is relatively localized. If a structural

change were propagating over a significant portion of the interface, one would expect a significant effect on the orientational structure of the surface water.

To address this question more directly, we examine the water structure within a solid angle of 54.8° (see Appendix E for a drawing). This region includes all surface waters within an arc length of $2\sigma_w$ from the dipole axis. The pair correlation function of the dipole with water oxygen was calculated for waters lying inside this solid angle. As the solute dipole is increased, a new peak emerges from the first hydration layer. Integration of this peak indicates that exactly one water molecule breaks free from the hydrogen bond network and shifts toward the solute. One expects that some level of strain is introduced in the neighboring molecules. The picture one arrives at is that two hydrogen bonds are broken, and the water oxygen, freed from the network, rotates and coordinates to the solute. This picture is supported by the value we obtained for the excitation free energy, $F_0 \simeq 7\ k_{\mathrm{B}}T$, which is approximately the enthalpy required to break two hydrogen bonds in SPC/E water[94].

The strain in the hydrogen bond network associated with the excitation is evident in the distribution of O-O-H angles between neighboring first shell water molecules inside the same solid angle. To define the hydrogen bond angle, we first take the line through the two oxygen nuclei; then, of the four associated hydrogen atoms, we choose the O-H bond that makes the smallest angle with the O-O line (see figure 3.10, inset). These distributions are shown for three different dipole moments in figure 3.10. The occupation of the buckled state with the larger hydrogen bond angle grows with increasing solute dipole moment. The definition used here for the hydrogen bond angle is borrowed from the work of Kim Sharp[88]. Similar distributions of hydrogen bond angles at interfaces of varying charge were seen by Sharp and cowork-

ers. However, that work so far only showed that the distribution becomes bimodal at charged interfaces, and the present study adds to this the finding that water can be made to switch between the different states, with significant implications for the hydration thermodynamics. In fact, it is a quite general property of water at interfaces that the electric fields from the solutes cause the water molecules to repopulate different states without significant changes to the states themselves[35]. A similar phenomenology has also been found in numerical simulations of a planar surface in contact with water, with a gradual increase in surface polarity[36].

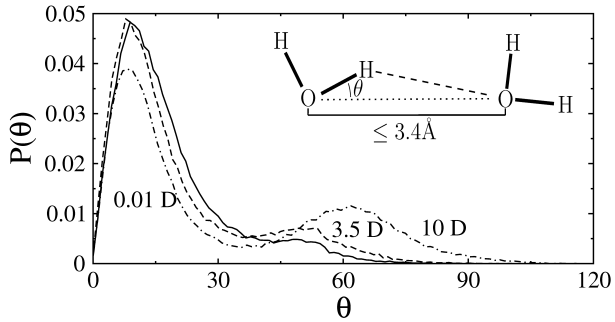

FIG. 3.10. Distributions of O-H-O angles θ for the RD10 configuration at m_0 equal to 0.01, 3.5, and 10 D. The distributions were calculated according to the algorithm suggested by Sharp *et al*[88] in the region of the first hydration layer within the solid angle cutting the circumference length of $2\sigma_s$ at the surface (see Appendix E). The inset shows the definition of the bond angle and the distance cutoff within which the angles were sampled.

V Discussion

We have presented here a study of the statistics of the electric field produced by hydration water inside a nanometer-sized solute. We find that these statistics are significantly altered when a dipole is placed on the solute, near the interface. As the dipole magnitude is increased, the surface waters respond by populating an excited state, which is higher in free energy than the ground state by approximately the energy needed to break two hydrogen bonds ($\simeq$ 7

$k_{\mathrm{B}}T$). The excited state is characterized by a domain of surface waters with a distorted hydrogen bond network. To put the water into the excited state, what is required is the field of a dipole approximately twice water's, located approximately one solvent diameter from the water closest approach radius. The electric field strength produced by this dipole at the interface puts the system at a crossover point with the system jumping between the two states, and characterized by strongly non-Gaussian fluctuations.

Because of the local nature of the excitations associated with this transition, the area characterized by the fluctuations in excess of linear response is actually quite broad, with significant populations of both states present for a range of solute dipoles. This is in contrast to what one observes for a bulk phase transition, which is characterized by global changes, strongly localized in thermodynamic parameter space. Accordingly, significant populations of the excited state could be reached with weaker perturbations, such as a hydroxyl or other polar functional group. The fields from small monatomic ions are expected to be strong enough to switch surface waters completely into the excited state.

The phenomena described here should be observable by optical probes. A probe near a water domain that predominantly exists in one state will record a spectral shift and spectral width that are proportional to the change in dipole moment of the probe and related by the general results of linear response. In contrast, a probe placed near a domain of water that is near the coexistence point of the two states will record a distinctly broadened spectral width, and an altered spectral shift. If good measurements of spectral widths can be performed, it should be possible to observe the breakdown of linear response for such a system. It should also be noted that the way in which this

transition manifests itself will depend on where the two electronic states lie on the plots in figure 3.7. If the two electronic states lie on opposite sides of the transition, an enhanced spectral shift will be observed, with a small change in the width. In contrast, any electronic state producing a domain of water close to the coexistence point will be characterized by a significantly broadened spectral line. In the case of real optical probes, the interface will likely present a mosaic of water domains in different states. For that reason, experiments could usefully be analyzed in terms of the ideas developed here, but results may be best understood as probing average properties of the hydration water. It should also be noted that without a large number of data points, the deviations from the predictions of simple linear solvation models will be difficult to detect by measurements of spectral shift, since if one has only a few points, the 'S' shape of the solvent response will likely appear as a line with some level of noise. The spectral width is therefore a much better probe of the local solvent structure than the spectral shift.

Our results also predict that Stokes shift dynamics will slow down when water is near the transition region, as seen in figure 3.7c. A nanoscale solute decorated by a mosaic of charges will then produce a dynamically heterogeneous Stokes shift response[72]. The dynamics observed here are still much faster (ps) than the slow dynamics observed in Stokes shift experiments on chromophores bound to proteins (ns) [95, 50, 96]. The difference of three orders of magnitude between the two suggests the possibility that the chemically heterogeneous surfaces of proteins can produce cooperative domains of several excitations. Alternatively, it can also be argued that all the slow dynamics of water at the protein-water interface are due to coupling of the water to protein

motions[51]. And it is of course possible that the overall response of biological water is best described as a combination of these effects[97].

Chapter 4

COOPERATIVE TRANSITION IN INTERFACIAL WATER

I Introduction

In chapter 3, we described the ability of water to switch discontinuously between different states at the interface with a nanometer-sized solute with a dipole introduced near the surface; we studied the effect of this switching between states on the electrostatics of hydration. The question naturally arises of what happens differently when a nanoscale interface is decorated with a collection of multipoles. Specifically, we ask the question whether structural excitations in the hydration water can behave cooperatively, and what the implications are for solvation thermodynamics and dynamics. One can imagine several possible scenarios to address questions of the length scale of cooperativity between excitations, the effect of different charge distributions at the interface, and the interplay between the topology of the interface and the charge distribution. In the present study, we address the more modest goal of demonstrating that such cooperativity is possible, and that the implications are significant for understanding the hydration of nanometer sized objects. We ask here what will be observed when the entire surface of a nanometer sized solute is decorated with dipoles. Will the solvent response show a crossover, as with the single dipole? Will the nature of this crossover be the same, or will new features emerge as a result of the collective response of the hydration layer? How will this manifest itself in the electrostatic, thermodynamic and dynamic properties of the solution?

To study the response of water at a nanoscale interface to a collection of perturbing dipoles, we study a system having the geometry of C_{180} fullerene. We introduce point dipoles on each carbon atom, oriented so that the dipole moment direction is along the radius vector (the vector from the center of mass of the fullerene to the carbon atom). We simulated this system by molecular dynamics using the NAMD 2 package [98] with 37924 hydration waters. Water was represented by the SPC/E model [75]. For the Lennard-Jones interactions of the fullerene carbon with water oxygen, the AMBER atom type CA[99] was used, with the Lennard-Jones radius given by the arithmetic combination rule, and the Lennard-Jones well depth given by the geometric combination rule. We simulated systems with the carbon dipole magnitude ranging between 0.5 Debye and 9.0 Debye. Following 10 ns equilibration, we simulated each system for 40 ns at 310 Kelvin. Further simulation details are given in Appendix G.

II Results

We first examine the dependence of the solute-solvent electrostatic energy, u_{0s} on the strength of the dipole moment, m_C. This quantity is easy to compare to the results from the Kihara solute with single dipole, presented in chapter 3. We define the reduced solute-solvent energy, scaled to reflect the magnitude of the electrostatic energy between the carbon dipole and the surface water dipoles:

$$u^*_{0s} = u_{0s} \times \frac{r^3_{Cs}}{m_C m_s}, \tag{4.1}$$

where u_{0s} is the total electrostatic solute-solvent energy, m_C is the magnitude of the dipole moment placed on the carbon atoms, m_s is the dipole moment of SPC/E water, 2.351 D, and r_{Cs} is the distance from the carbon dipoles to the interface. In accordance with the estimate of the continuum radius in our

work on the Kihara solutes in chapter 3, we use the value, $r_{Cs} = \sigma_{CO} - 0.5$Å = 2.86 Å, where σ_{CO} is the Lennard-Jones diameter for fullerene carbon interacting with SPC/E oxygen. We present the average and variance of u^*_{0s} in figure 4.1; the solid squares represent the results from the present study of C_{180}; we scale these by the factor 1/180, in order to compare to the results for the Kihara solute. The x-axis in figure 4.1 is the reduced dipole moment, $m^* = (m_C/m_s) \times (\sigma_s/r_{Cs})^3$. The hollow squares and hollow circles show the results of the Kihara plus dipole study, with $r_d = 9$ Å and $r_d = 10$ Å, respectively. The results for the C_{180} solute follow the behavior seen for the Kihara study, for small magnitudes of m_C. This is consistent with the picture that individual structural excitations in the solvent are uncorrelated, so that the average behavior reflects the behavior seen for a single perturbation. However, as the perturbing dipoles are increased further, a second peak emerges in the variance. This second broad peak seems to correspond to the emergence of cooperative switching between states in the hydration shell.

In figure 4.2, we also show the result for the non-Gaussianity parameter, $\chi_G = -\beta\langle(\delta u_{0s})^2\rangle/\langle u_{0s}\rangle$. This parameter goes through two distinct peaks. The indication is that the fluctuations are in excess of the expectations of linear response for a very broad range of surface polarity.

To understand the physical origin of these observations, we examine the first and second orientational parameters of the surface waters. We consider waters with the center of mass at distances less than 8.5 Å from the solute center. We define the order parameters as in chapters 2 and 3; the results are presented in figure 4.3. The first orientational parameter, indicated by the open circles, is small and positive for small m_C. With increasing dipole moment, p_1^I decreases in two features, until ending at $p_1^I \approx -0.25$. We also find

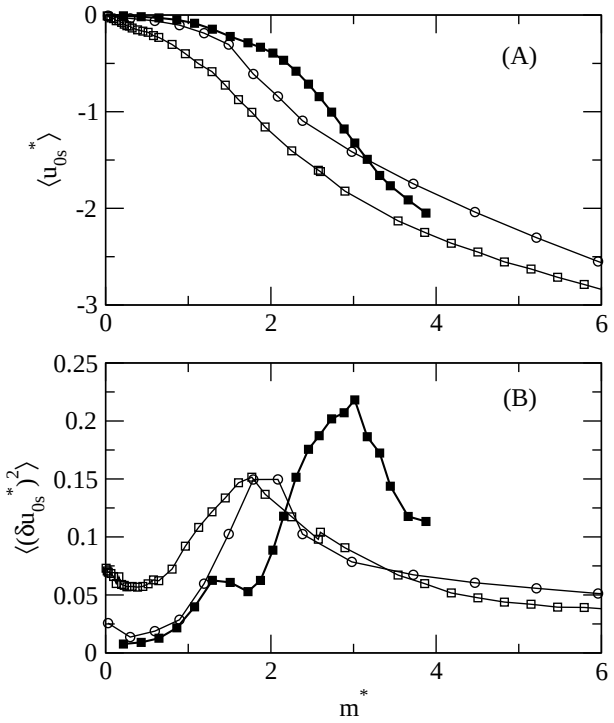

FIG. 4.1. Average (A) and variance (B) of the reduced solute-solvent, electrostatic energy u^*_{0s}. The solid squares correspond to the results from the present study. For context, the results for the Kihara solute with a perturbing dipole at locations $r_d = 9$Å and $r_d = 10$Å are indicated respectively by the open squares and open circles.

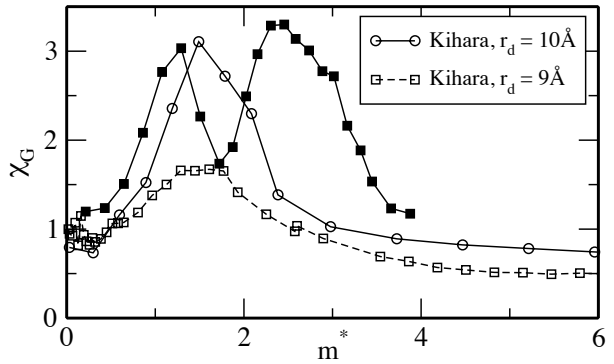

FIG. 4.2. Non-Gaussian parameter $\chi_G = -\beta\langle(\delta u_{0s})^2\rangle/\langle u_{0s}\rangle$. The solid squares correspond to the results from the present study. For context, the results for the Kihara solute with a perturbing dipole at locations $r_d = 9$ Å and $r_d = 10$ Å are indicated respectively by the open circles and open triangles.

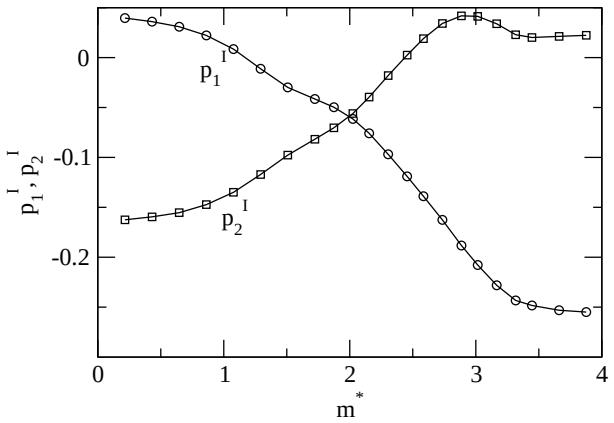

FIG. 4.3. First and second orientational order parameters,p_1^I and p_2^I for the first shell waters. The open circles and open squares represent, respectively the first and second parameters.

two features in the behavior of the second orientational parameter, p_2^I (open squares in figure 4.3). This parameter starts at a negative value for small m_C, indicating the preference of waters to orient in the plane. With increasing m_C, p_2^I decreases in magnitude with a weak shoulder at $m_C \approx 3.5$ to 4.0 D ($m^* \approx 1.5$). as the carbon dipoles increase further, the second orientational parameter crosses zero and passes through a peak, then levels off at a small, positive value, indicating a weak preference for orientation of the water dipoles along the radial direction.

The negative values of p_1^I for large solute dipoles indicate surface water dipoles oriented somewhat against the dipoles placed on the carbon atoms. This seemingly counterintuitive result is easily understood from the arrangement of water molecules around fullerenes. Greater surface area contact and more favorable packing are achieved when waters occupy the area near the centers of the faces of a fullerene[100]. Consequently, in our system, the waters are sensitive mostly to the equatorial electric field from the carbon dipoles. As a result, the waters tend to point opposite the dipoles placed on the solute. The difference observed here, compared with what was found for the Kihara

solute with the dipole placed near the surface, highlights the effect the solute topology can have on the orientational properties of the interfacial waters.

If the second transition observed in this progression is indeed the result of cooperative rearrangement of the interface waters, one expects to see this reflected in the dynamics. We consider first the self time correlation function, $C_1(t) = \langle (p_1^I(t) p_1^I(0) \rangle$, where $p_1^I(t)$ is the instantaneous value of the order parameter p_1^I. We fit the resulting function to a sum of two exponentials. The faster of the two has a timescale of approximately 0.2 to 0.5 ps, consistent with the dynamics of bulk SPC/E water [101]. We plot the time constant τ_E of the slower exponential in figure 4.4, indicated by the solid squares. The timescale spikes to the nanosecond range in the vicinity of the second transition, much like the phenomenology of a first order phase transition; after the spike, the sudden drop of the relaxation time occurs at higher dipole moments than the maximum in fluctuations, reminiscent of spinodal decomposition [102, 103]. We also calculated the autocorrelation function for the electrostatic solute-solvent energy. We analyze the dynamics in the same way, and the results are shown in figure 4.4 by the open circles. The dynamics of the hydration energy follow the dynamics of the orientational motion in the hydration layer (figure 4.4).

The transition is accompanied by a change in the water density around the solute. Waters in the excited state are notably closer to the solute than those occupying the state with the dipoles oriented in the plane of the solute-water interface. In figure 4.5, we show the mean number of waters within 8.5 Å of the solute center N_1, with increasing dipole moment. As the excited state population increases, the number of waters within this distance cutoff

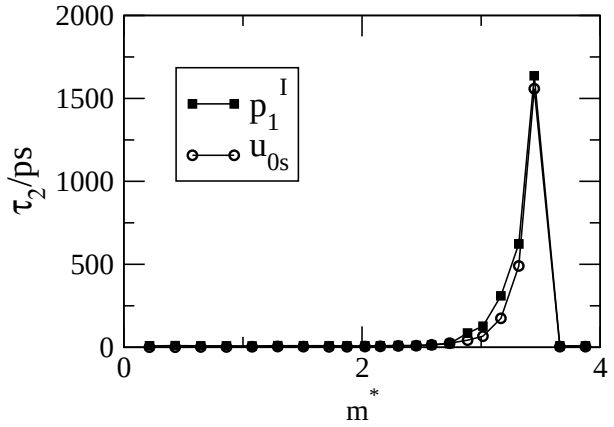

FIG. 4.4. Exponential relaxation time, τ_2, of the slow component of the relaxation of the orientational parameter p_1^I (solid squares) and of the electrostatic solute-solvent energy u_{0s} (open circles).

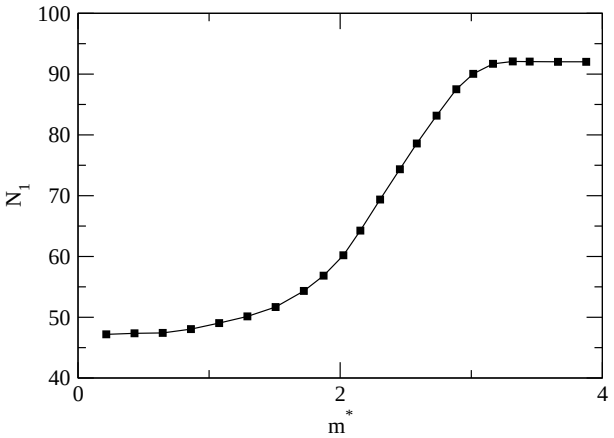

FIG. 4.5. Number of waters with oxygen within 8.5 Å of the solute center of mass. The number increases as the system goes through the crossover, then levels off as the excited state is saturated.

increases and as the transition completes, the number of waters in the first shell saturates.

III Chemical Potential

The solute-solvent interaction energy is an easy quantity to calculate, but is not directly observable. However, one can determine the chemical potential

of electrostatic solvation of the fullerene by thermodynamic integration[13, 14].

$$\mu_{el} = \int_0^1 \, d\lambda \, \left\langle \left(\frac{\partial u_{0s}}{\partial \lambda} \right) \right\rangle_\lambda , \tag{4.2}$$

where μ_{el} is the electrostatic chemical potential, u_{0s} is the electrostatic solute-solvent energy, and $\lambda = m/m_C$.

For the case of turning on the carbon dipoles, we write the total solute-solvent electrostatic energy as $u_{0s} = -\sum_i \mathbf{m}_i \cdot \mathbf{E}_i = -m \, \sum_i \hat{\mathbf{m}}_i \cdot \mathbf{E}_i$, where $\mathbf{m}_i$ is the dipole moment on the ith carbon, and $\mathbf{E}_i$ is the solvent electric field at the ith carbon. Then for the integration, we get:

$$\mu = \int_0^{m_C} \mathrm{d}m \; u_{0s}(m)/m. \tag{4.3}$$

Within linear response, this gives: [14, 9, 104]

$$\mu = u_{0s}/2 \propto (m_C)^2. \tag{4.4}$$

However, the response we see here is clearly non-linear (see figure 4.1), so that we calculate the chemical potential here from numerical integration of equation 4.3. We have performed this analysis for our C_{180} solute, with the results given in figure 4.6a. We plot the reduced chemical potential, $\mu^* = \mu r_{Cs}^3/(m_C)^2$. Within linear response, this will be constant with changing m_C. What we find is that the chemical potential scales very roughly with m_C^2 only for small dipoles, up to about 2 D, before increasing in magnitude significantly faster than m_C^2. The scaling for larger dipoles is approximately third order in m_C, as can be seen from the bottom panel, figure 4.6b, which shows the log-log plot of μ^* vs. m^*. For large dipole moments, the slope of $\ln(\mu^*)$ with $\ln(m^*)$ is about 1.5, indicating a scaling of $\mu \sim (m_C)^{3.5}$.

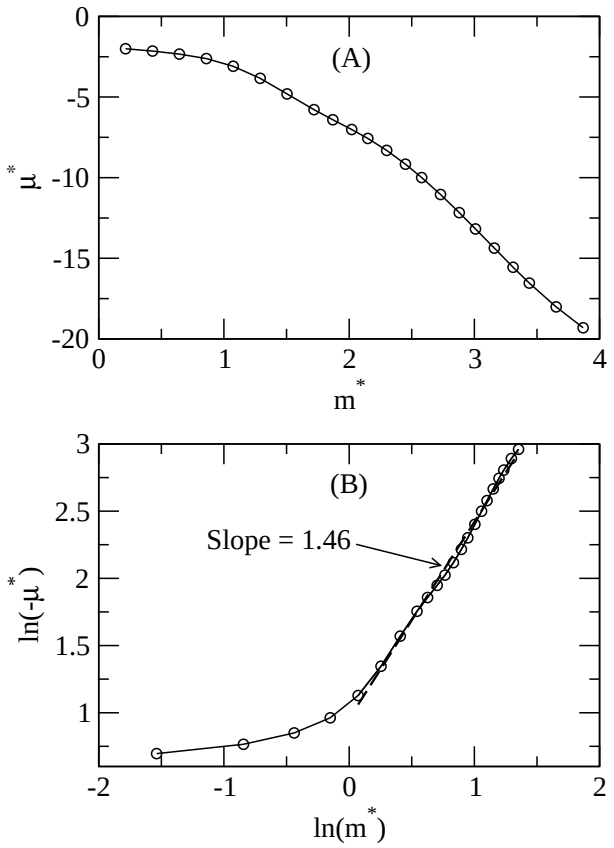

FIG. 4.6. Electrostatic chemical potential of the C_{180} solute calculated from thermodynamic integration. The top panel (A) shows the reduced chemical potential, $\mu^* = \mu r_{Cs}^3 / m_C^2$; this quantity is constant in the case of linear solvation. The x-axis is the reduced dipole, $m^* = (m_C/m_s)(\sigma_s/r_{Cs})^3$. The bottom panel (B) shows the log-log plot of μ^* vs. m^*; the slope gives the scaling of μ with the carbon dipole strength.

IV Discussion

The results presented here indicate that the structural excitations induced in the waters near the interface with a nanometer size object can behave in a cooperative manner, switching between different collective states. Near the point of transition, the associated solvation dynamics become quite slow, with timescales reaching nanoseconds. While the dynamics become cooperative, the broadness of the transition observed implies that the structural changes still must still be fairly limited in size. The whole hydration layer does not flip between states in a concerted manner.

Because of the tendency of interface waters to occupy the faces of the fullerene, the excited state studied here actually represents the opposite side of the curve obtained in our previous study of the Kihara solute with a single point dipole. This confirms that such a state exists and also emphasizes that the specific structural changes in water at real interfaces will be quite sensitive to both the charge distribution and the topology.

It was recently suggested that biomolecules place water near the critical point of the weak dewetting transition associated with hydrophobic solvation [7]. Our present results indicate the existence of another critical point, between hydrophobic and hydrophilic hydration of nanometer-sized objects that may also be important for biology. The fluctuations at a nanoscale interface can likely be tuned by adjusting the charge density and distribution. This points to a possible link between protein function and protein structure.

Linear solvation models are expected to fail for hydration of nanometer-sized solutes, over a broad range of surface polarity, where the chemical po-

tential of a collection of multipoles scales approximately third order with the surface polarity.

Chapter 5

FREE ENERGY SURFACE OF ELECTRIC POTENTIAL FLUCTUATIONS AT THE REDOX SITE OF CYTOCHROME B562 BY UMBRELLA SAMPLING

I Introduction

The condition of linear response relating the Stokes shift of electron transfer to the fluctuations of the energy gap and to the free energy of electron transfer poses significant difficulties for understanding energy flow in biology [62, 5]. The fact that photosynthesis works implies that the ordinary consequences of linear response theory must not apply to at least some redox proteins. The issue has been addressed by the introduction of a rate dependent reorganization energy of electron transfer[62], and by the idea that the statistics of electric potential fluctuations at redox sites may be significantly non-Gaussian[5]. Several redox proteins have been shown to undergo very large fluctuations of the energy gap for the redox half reaction, far in excess of what is expected based on the requirements of bioenergetics. In further cases, the remarkably large reorganization energy from fluctuations, λ^{var}, has been shown to be far in excess of the reorganization energy determined from the Stokes shift, λ^{St}. Unfortunately, the possibility of generating improved, non-linear models for biological electron transfer has been hindered because the free energy surfaces of electron transfer are not known for any of the proteins that have been found to exhibit these large electrostatic fluctuations. In this work, we sought to generate such a surface, in order to aid in generating an

analytical model for electron transfer beyond the formalism of linear response and Marcus theory. The surfaces we generate in the present study are not intended to correspond to one particular redox process in the electron transfer chains in biology. Our goal here is to probe the statistics of electric potential fluctuations at the redox site.

We study here the protein cytochrome B562. This redox protein was chosen because the fluctuations of the electric potential due to water at the heme iron were shown in a recent study to correspond to a reorganization energy of 21.5 eV [96]. The protein structure was built from from the protein data bank (PDB) structure 256B. The molecular dynamics package NAMD[98] was used with the CHARMM all atom force field[105], and the protein was hydrated in 33268 TIP3P water molecules. We perform umbrella sampling of the statistics of the electric potential at the heme iron, by adding an extra charge δq to the iron. Simulations were performed for values of δq between -0.6 and 1.6, in increments of 0.2. The addition of the charge δq effectively introduces the biasing potential, $\Delta U = -\delta q \phi$, where ϕ is the electric potential at the heme iron. The unbiased free energy surfaces, $F(\phi)$ can then be reconstructed using the weighted histogram analysis method (WHAM)[106, 107]. In order to maintain system neutrality, an extra charge $-\delta q$ was added to one counterion. Further simulation details are given in Appendix H.

II Results

The free energy surfaces, $F(\phi)$ obtained for the fluctuations of the electric potential at the iron are shown for both the reduced ($\delta q = 0$, indicated 'RED') and oxidized ($\delta q = 1$, indicated 'OX') states in figure 5.1. The surface obtained for the reduced state is nearly parabolic, with the corresponding, variance of

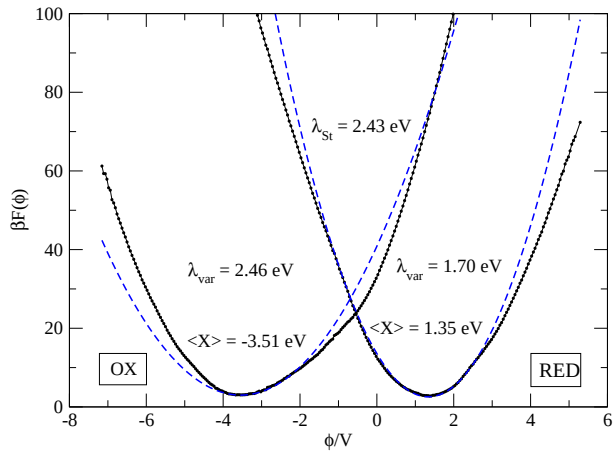

FIG. 5.1. Free energy surfaces, $F(\phi)$ for the RED ($\delta q = 0$) and OX ($\delta q = 1.0$) states. The reorganization energies from fluctuations for the two states are indicated along with the reorganization energy from the Stokes shift. The solid lines are the free energy surfaces determined from WHAM, and the dashed lines correspond to parabola fits to the bottom of the curves.

the potential equal to 0.0909 V^2. This width corresponds to a value of $\lambda^{var} =$ 1.70 eV. In contrast, the surface obtained for the oxidized state is flattened near the minimum; the shape is not described well by a parabola, and the variance corresponds to the value, $\lambda^{var} = 2.46$ eV. The Stokes shift obtained for the system is 4.86 eV, corresponding to $\lambda^{St} = 2.43$ eV, approximately equal to the reorganization energy obtained from fluctuations for the reduced state, but significantly smaller than that for the oxidized state.

To take a closer look at the larger fluctuations observed around $\delta q = 1$, we can look at the free energy surfaces, $F(\phi)$ at different values of the perturbation, δq (figure 5.2). Following the progression from $\delta q = -0.6$ through $\delta q = 1.6$, we see that for the most part the free energy surfaces are approximately parabolic, corresponding to a range of electric potential fluctuations over which the statistics are approximately Gaussian. However, in the vicinity of $\delta q = 1$, a flat region appears in the surface. At $\delta q = 0.8$, the flat part of the curve is approximately at the bottom of the well, corresponding to maxi-

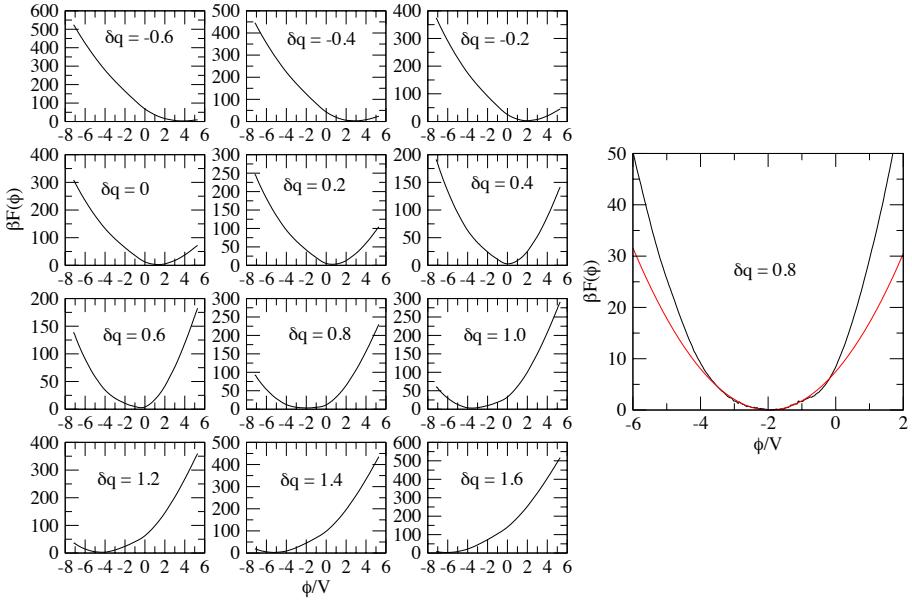

FIG. 5.2. Free energy surfaces $F(\phi)$ for different values of δq. As one follows the progression from $\delta q = -0.6$ all the way through to $\delta q = 1.6$, we see mostly surfaces that are approximately parabolic near the bottom. However, in the vicinity of $\delta q = 0.8$, we observe a flat region of the surface. This flattened portion of the free energy surface has a significant effect on the variance of the electric potential, only when it is reachable within a few kT of the minimum of the free energy surface. The zoomed plot to the right shows the detail for the free energy surface at $\delta q = 0.8$. The black line is the free energy surface from WHAM and the red line is the parabola fit to the bottom of the curve.

mum fluctuations of the electric potential, and maximum deviation from the predictions of linear response. For reference, table 5.1 shows the values of the variance of the potential for the sequence of δq. The variances are normalized to the variance at $\delta q = 0$.

The effect is, however, fairly subtle. For all values δq, we obtained a significantly smaller value of λ^{var} than predicted. To understand the source of this surprise, we examine the fluctuations of the potential due to different components of the system. In figures 5.3 (RED) and 5.4 (OX), we show the distributions of the electric potential at the heme due to water, due to the protein, and due to the ions. The distribution of the total potential is also shown. The distributions due to the individual components are actually quite

Table 5.1. Variance of the electric potential at the heme iron for the series of charge perturbations, δq. The quantities are normalized to the variance at $\delta q = 0$.

δq	$\langle(\delta\phi)^2\rangle_{\delta q}$ / $\langle(\delta\phi)^2\rangle_{\delta q=0}$
-0.6	1.7
-0.4	1.4
-0.2	0.92
0.0	1
0.2	0.97
0.4	0.72
0.6	0.93
0.8	3.2
1.0	1.4
1.2	1.2
1.4	1.2
1.6	1.2

broad. Table 5.2 gives gives the variances obtained for the individual components, in terms of the energies $\lambda_i^{var} = e\beta\langle(\delta\phi_i)\rangle/2$, where e is the elementary charge and i stands for the component of the system, either water, protein or ions. The value obtained for water λ_w^{var} is quite large. However, there is clearly a significant amount of cancellation between fluctuations from the individual components, so that the total variance is more modest. In particular, we note that for the system studied here, the ions are a major source of fluctuations of the potential. This is in contrast to what was obtained previously for plastocyanin[62]; in that case, the potential due to the ions in the simulation

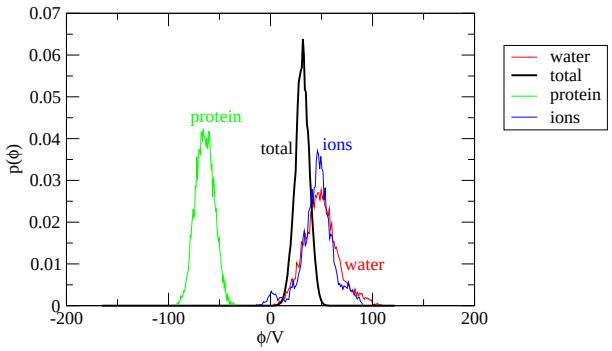

FIG. 5.3. Distribution of the electric potential at the heme iron for the RED state ($\delta q = 0$). In addition to the overall distribution, the distributions of the components due to water, protein and ions are also shown.

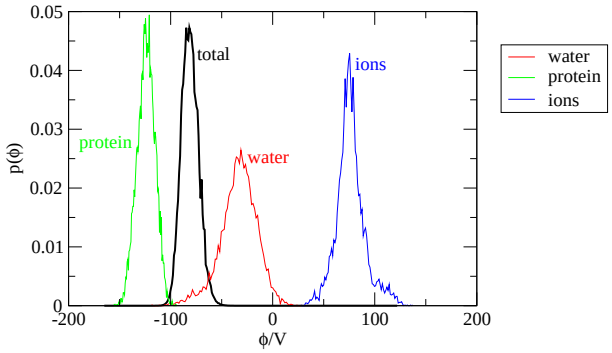

FIG. 5.4. Distribution of the electric potential at the heme iron for the OX state ($\delta q = 1$). In addition to the overall distribution, the distributions of the components due to water, protein and ions are also shown.

turned out to be almost constant, not contributing significantly to the overall reorganization energy.

The contributions of the different parts of the system to the overall Stokes shift are shown in table 5.3. Particularly noteworthy is the significant contribution from the ions. Theoretical studies predict the contribution to the Stokes shift from ions to be on the order of 0.01 eV. [108], and the observation of an ion contribution orders of magnitude larger than this raises doubts about the effectiveness with which the ionic atmosphere is modeled in finite size simulations.

Table 5.2. Variance of the electric potential at heme iron, due to all sources (λ^{var}), water (λ_w^{var}), protein (λ_p^{var}), and ions (λ_I^{var}), shown for $\delta q = 0$ (RED) and $\delta q = 1$ (OX). All values are in eV.

state	λ^{var}	λ_w^{var}	λ_p^{var}	λ_I^{var}
RED	1.7	9.7	3.0	9.0
OX	2.5	12.	2.6	7.1

Table 5.3. Contributions to the total Stokes shift from various components of the system. The data are in eV; the subscripts w, p and I refer respectively to the contributions from water, protein and ions.

ΔX	ΔX_w	ΔX_p	ΔX_I
4.86	3.60	2.60	-1.32

III Discussion

Our original goal in this work was to generate a free energy surface for a redox protein that shows significantly non-Gaussian statistics of the fluctuations of the electric potential at the redox site. That free energy surface was intended to serve as a model for understanding biological electron transfer and to aid in producing an analytical model of the fluctuations at a redox site due to hydration water. What we find is that it is not clear what the intrinsic behavior of water would be at the interface with our solute in the present study, since the ions make a significant contribution to the overall picture. Of course, understanding the role of ions in bioenergetics is important, but this constitutes a further complication we do not aim to address at this time.

Our results have shown that the system setup chosen for this work was not well suited to our goals, so that further pursuit of this project will require significant rethinking. It is possible to simulate the system with fewer ions present, but whether that will change the overall picture is not clear. Another possible solution is to simulate the system non-neutral. Although the Ewald

sum is divergent in this case, it is possible to apply the correction to account for the self-interaction of the system and its images[21].

The present results raise pragmatic concerns over setting up biomolecular simulation. The large Stokes shift from ions observed here may be the result of the extra charge added to the system to maintain neutrality. Or it may simply be an artifact of the force field used. The behavior of ions in simulation is notably strongly dependent on force field parameters[109, 110]. Therefore, the observation of a significant contribution of ions to the quantities of interest indicates the fundamental difficulty of obtaining "realistic" results for such a system by molecular dynamics. We therefore emphasize that our goal in such a project is to generate results for models with interesting behavior, in order to map out the range of possible behaviors. It remains for experimentalists to determine where specific systems fall in the range of possibilities.

Nevertheless, there are some points we learn from this set of simulations. We have here at least one example of a case in which linear response is followed relatively closely. We find that linear response is successful in the region near $\delta q = 0$. We also note that the degree of nonlinearity observed in a charge transfer process depends not only on whether the free energy surfaces are nonlinear, but also on where the two states of interest lie on that curve.

Chapter 6

CONCLUSION

In our studies of water at the interface with nanometer-size solutes, we have examined several properties, with an emphasis on the electrostatic properties of the hydration layer. We have found that the polarity of water at the interface is enhanced when compared to bulk water[23]. We quantify this polarity in terms of the dielectric response of the hydration layer. The increased polarity can be traced back to the increased density of water at the interface. Even in the case of a hydrophobic solute that undergoes weak dewetting at the interface, the collective dielectric response of the hydration layer is enhanced, compared with bulk water. The implication is that one cannot effectively model aqueous solutions as a simple superposition of components with different dielectric constants, separated by a mathematical interface, as suggested by continuum electrostatics. Depending on the question one asks, the effect may or may not be critical. We find that the chemical potential of a dipole at the center of a spherical solute in water approaches the prediction of continuum electrostatics as the solute size increases. This is in contrast to what was found previously for dipolar hard spheres, and it may therefore be due to the strength of hydrogen bonds. On the other hand, the energy stored in the electric field in the hydration layer of a nanometer size solute is expected to be enhanced compared to the prediction of continuum electrostatics.

In contrast to solvation of a multipole at the center of the cavity, we have found that when the statistics of the electric field fluctuations are probed near the solute-water interface, the statistics become strongly non-Gaussian [111].

The result is an excess in fluctuations of the electric field at the interface. This is the result of interfacial waters switching between different preferred orientations. The excess fluctuations are associated with slow hydration dynamics. The region of excess fluctuations is quite broad, so that one expects the phenomenon to be present in the hydration shells of a variety of solutes with surface polar groups.

We have found, further, that when the interface is decorated with a collection of dipoles, the region characterized by excess fluctuations becomes broader still. This phenomenon is due to the onset of a second, cooperative transition in the interfacial waters. The excess fluctuations associated with the two transitions in the interfacial water lead to a broad range of dipole magnitudes over which the scaling of the hydration free energy is approximately cubic, rather than quadratic as continuum (or any linear response) models would predict. This implies that continuum treatments of nanometer sized solutes with polar domains at the interface will have the picture qualitatively wrong. Consequently, even when continuum models are calibrated, they cannot be expected to be robust. The solvation dynamics become quite slow, when the hydration layer cooperatively switches between configurational states, spiking to the nanosecond timescale in the vicinity of the transition.

The results have implications for biology. The nature of the hydration of redox proteins is critical for understanding the energetics of biological electron transfer. The traditional picture of charge transfer reactions assumes the solvent behaves like a dielectric in the linear regime. The observation of fluctuations significantly in excess of the predictions of linear response for systems with a significant polarity at the surface implies that this treatment is not based on the right picture. Protein surfaces are characterized by regions of

high and low charge density; one therefore expects the overall solvation picture to involve a combination of hydrophobic solvation (approximately harmonic) and of the picture painted here of stronger scaling of the solvent response with the solute polarity. The breaking of linear response implies that charge transfer in biology may be more energetically efficient than the traditional picture of redox would predict. Simulations of hydrated proteins have already indicated a significantly non-Gaussian character of the fluctuations of the energy gap for biological electron transfer reactions[5]. We demonstrate here that such effects could be achieved, at least in part, due to water switching between preferred states at the interface. Most likely, this is only one part of the picture for biological systems. The slow protein dynamics are known to couple to the hydration water[97, 51], and seem to account for at least a significant portion of the slow hydration dynamics. But a recent study of GFP has shown that when the protein is frozen, a degree of non-Gaussianity is retained in the solvent response at the chromophore[68].

REFERENCES

[1] P. Ball, Chem. Rev. **108**, 74 (2008).

[2] P. L. Privalov, Crit. Rev. Biochem. Mol. Biol. **25**, 5910 (1990).

[3] P. W. Fenimore, H. Frauenfelder, B. H. McMahon, and F. G. Parak, Proc. Natl. Acad. Sci. **99**, 16047 (2002).

[4] N. Muneda, M. Shibata, M. Demura, and H. Kandori, J. Am. Chem. Soc. **128**, 6294 (2006).

[5] D. N. LeBard and D. V. Matyushov, Phys. Chem. Chem. Phys. **12**, 15335 (2010).

[6] C. A. Angell, Nat. Mater. **11**, 362 (2012).

[7] A. J. Patel *et al.*, J. Phys. Chem. B **116**, 2498 (2012).

[8] S. Sarupria and S. Garde, Phys. Rev. Lett. **103**, 037803 (2009).

[9] D. Ben-Amotz and R. Underwood, Acc. Chem. Res. **41**, 957 (2008).

[10] T. L. Beck, J. Stat. Phys. **145**, 335 (2011).

[11] P. M. Chaikin and T. C. Lubensky, *Principles of condensed matter physics* (Cambridge University Press, Cambridge, 1995).

[12] D. R. Martin and D. V. Matyushov, Phys. Rev. E **78**, 041206 (2008).

[13] J. P. Hansen and I. R. McDonald, *Theory of Simple Liquids* (Academic Press, Amsterdam, 2003).

[14] H.-A. Yu and M. Karplus, J. Chem. Phys. **89**, 2366 (1988).

[15] H. Fröhlich, *Theory of dielectrics* (Oxford University Press, Oxford, 1958).

[16] M. Born, Z. Phys. **1**, 45 (1920).

[17] L. Onsager, J. Am. Chem. Soc. **58**, 1486 (1936).

[18] C. J. F. Böttcher, *Theory of Electric Polarization* Vol. 1 (Elsevier, Amsterdam, 1973).

[19] S. Rajamani, T. Ghosh, and S. Garde, J. Chem. Phys. **120**, 4457 (2004).

[20] H. S. Ashbaugh, J. Phys. Chem. B **104**, 7235 (2000).

[21] G. Hummer, L. R. Pratt, and A. E. Garcia, J. Phys. Chem. **100**, 1206 (1996).

[22] W. M. Latimer, K. S. Pitzer, and C. M. Slansky, J. Chem. Phys. **258**, 349 (2000).

[23] A. D. Friesen and D. V. Matyushov, Chem. Phys. Lett. **511**, 256 (2011).

[24] J. M. J. Swanson, S. A. Adcock, and J. A. McCammon, J. Chem. Theory Comput. **1**, 484 (2005).

[25] M. Uematsu and E. U. Franck, J. Phys. Chem. Ref. Data **9**, 1291 (1980).

[26] E. Condon, Phys. Rev. **28**, 1128 (1926).

[27] A. Nitzan, *Chemical Dynamics in Condensed Phases* (Oxford University Press, New York, 2006).

[28] D. V. Matyushov and M. D. Newton, J. Phys. Chem. A **105**, 8516 (2001).

[29] N. Mataga, Y. Kaifu, and M. Koizumi, J. Am. Chem. Soc. **29**, 465 (1956).

[30] E. L. Mertz, V. A. Tikhomirov, and L. I. Krishtalik, J. Phys. Chem. A **101**, 3433 (1997).

[31] L. D. Landau and E. M. Lifshitz, *Electrodynamics of continuous media* (Pergamon, Oxford, 1984).

[32] M. Neumann, J. Chem. Phys. **82**, 5663 (1985).

[33] M. Neumann, Mol. Phys. **57**, 97 (1986).

[34] M. Neumann, Chem. Phys. Lett. **95**, 417 (1983).

[35] C. Y. Lee, J. A. McCammon, and P. J. Rossky, J. Chem. Phys. **80**, 4448 (1984).

[36] N. Giovambattista, P. G. Debenedetti, and P. J. Rossky, Chem. Phys. **258**, 349 (2000).

[37] G. M. Torrie and G. N. Patey, J. Phys. Chem. **97**, 12909 (1993).

[38] K. A. Sharp and J. M. Vanderkooi, Acc. Chem. Res. **43**, 231 (2010).

[39] P. J. Rossky and J. D. Simon, Science **370**, 263 (1994).

[40] Y. R. Shen and V. Ostroverkhov, Chem. Rev. **106**, 1140 (2006).

[41] G. Hummer, S. Garde, A. E. Garcia, and L. R. Pratt, Chem. Phys. **258**, 349 (2000).

[42] S. Garde, G. Hummer, A. E. García, M. E. Paulaitis, and L. R. Pratt, Phys. Rev. Lett. **77**, 4966 (1996).

[43] K. Lum, D. Chandler, and J. Weeks, J. Phys. Chem. B **103**, 4570 (1999).

[44] T. R. Jensen *et al.*, Phys. Rev. Lett. **90**, 086101 (2003).

[45] G. Hummer and S. Garde, Phys. Rev. Lett. **80**, 4193 (1998).

[46] D. M. Huang and D. Chandler, J. Phys. Chem. B **106**, 2047 (2002).

[47] R. Jimenez, G. R. Fleming, P. V. Kumar, and M. Maroncelli, Nature **369**, 471 (1994).

[48] S. K. Pal and A. H. Zewail, Chem. Rev. **104**, 2099 (2004).

[49] O. Kwon, T. H. Yoo, C. M. Othon, J. A. Deventer, and A. H. Zewail, Trans. Faraday Soc. **57**, 557 (1961).

[50] J. Tripathy and W. F. Beck, J. Phys. Chem. B **114**, 15958 (2010).

[51] B. Halle and L. Nilsson, J. Phys. Chem. B **113**, 8210 (2009).

[52] R. A. Marcus, J. Chem. Phys. **24**, 966 (1956).

[53] R. A. Marcus, J. Chem. Phys. **26**, 867 (1957).

[54] N. S. Hush, Trans. Faraday Soc. **57**, 557 (1961).

[55] D. V. Matyushov, Chem. Phys. **351**, 46 (2008).

[56] R. A. Marcus, J. Chem. Phys. **24**, 979 (1956).

[57] A. Warshel, J. Phys. Chem. **86**, 2218 (1982).

[58] J. C. Rasaiah and J. Zhu, J. Chem. Phys. **129**, 214503 (2008).

[59] M. Cascella, A. Magistrato, I. Tavernelli, P. Carloni, and U. Rothlisberger, Proc. Natl. Acad. Sci. **103**, 19641 (2006).

[60] E. Solomon, R. Szilagyi, S. DeBeerGeorge, and L. Basumallick, Chem. Rev. **104**, 419 (2004).

[61] A. Warshel and W. W. Parson, Quat. Rev. Biophys. **34**, 563 (2001).

[62] D. N. LeBard and D. V. Matyushov, J. Phys. Chem. B **112**, 5218 (2008).

[63] D. N. LeBard and D. V. Matyushov, J. Phys. Chem. B **113**, 12424 (2009).

[64] H. B. Gray and J. R. Winkler, Proc. Natl. Acad. Sci. **102**, 3534 (2005).

[65] I. Muegge, P. X. Qi, A. J. Wand, Z. T. Chu, and A. Warshel, J. Phys. Chem. B **101**, 825 (1997).

[66] W. W. Parson, Z. T. Chu, and A. Warshel, Biophys. J. **74**, 182 (1998).

[67] P. K. Ghorai and D. V. Matyushov, J. Am. Chem. Soc. **127**, 16390 (2005).

[68] D. R. Martin and D. V. Matyushov, Non-gaussian statistics and nanosecond dynamics of electrostatic fluctuations affecting optical transitions in proteins, submitted,*J. Phys. Chem. B*.

[69] G. Hummer, L. R. Pratt, and A. E. Garcia, J. Phys. Chem. A **102**, 7885 (1998).

[70] D. Chandler and J. P. Garrahan, J. Chem. Phys. **123**, 044511 (2005).

[71] D. Chandler, Nature **437**, 640 (2005).

[72] N. Giovambattista, C. F. Lopez, P. J. Rossky, and P. G. Debenedetti, Proc. Natl. Acad. Sci. **105**, 2274 (2008).

[73] M. S. A. Kader, Chem. Phys. **281**, 49 (2002).

[74] T. Kihara, Rev. Mod. Phys. **25**, 831 (1953).

[75] H. J. C. Berendsen, J. R. Grigera, and T. P. Straatsma, J. Phys. Chem. **91**, 6269 (1987).

[76] W. Smith and T. R. Forester, J. Molec. Graphics **14**, 136 (1996).

[77] R. Schmid and D. V. Matyushov, J. Phys. Chem. **99**, 2393 (1995).

[78] J. Mittal and G. Hummer, Proc. Natl. Acad. Sci. **105**, 20130 (2008).

[79] V. P. Sokhan and D. J. Tildesley, Mol. Phys. **92**, 625 (1997).

[80] A. Papazyan and A. Warshel, J. Chem. Phys. **107**, 7975 (1997).

[81] V. Ballenegger and J.-P. Hansen, J. Phys. Chem. **122**, 114711 (2005).

[82] H. K. W. Y. Martin, D. W. Abraham, Appl. Phys. Lett. **52**, 1103 (2007).

[83] T. Fukuma, Sci. Tech. Adv. Mater. **11**, 033003 (2010).

[84] T. Uchihashi, M. Higgins, Y. Nakayama, J. E. Sader, and S. P. Jarvis, Sci. Tech. Adv. Mater. **16**, S49 (2005).

[85] T. Hiasa *et al.*, J. Phys. Chem. C **14**, 21423 (2010).

[86] M. Tachiya, Chem. Phys. Lett. **203**, 164 (1993).

[87] L. D. Landau and E. M. Lifshits, *Statistical Physics* (Pergamon Press, New York, 1980).

[88] K. A. Sharp and B. Madan, J. Phys. Chem. B **101**, 4343 (1997).

[89] C. Vega, E. Sanz, and J. L. F. Abascal, J. Chem. Phys. **122**, 114507 (2005).

[90] M. S. S. Challa, D. P. Landau, and K. Binder, Phys. Rev. B **34**, 1841 (1986).

[91] A. Laaksonen, P. G. Kusalik, and I. M. Svishchev, J. Phys. Chem. A **101**, 5910 (1997).

[92] R. Blinc and B. Žekŝ, *Soft modes in ferroelectrics and antiferroelectrics* (North-Holland Publishing Co., Amsterdam, 1974).

[93] K. Binder and D. W. Heermann, *Monte Carlo simulation in statistical mechanics* (Springer-Verlag, Berlin, 1992).

[94] D. van der Spoel, P. J. van Maaren, P. Larsson, and N. Timneanu, J. Phys. Chem. B **101**, 4343 (1997).

[95] P. Abbyad *et al.*, J. Phys. Chem. B **111**, 8269 (2007).

[96] D. V. Matyushov, J. Phys. Chem. B **115**, 10715 (2011).

[97] S. Sen, D. Andreatta, S. Y. Ponomarev, D. L. Beveridge, and M. A. Berg, J. Am. Chem. Soc. **131**, 1724 (2009).

[98] J. C. Philips *et al.*, J. Comput. Chem. **26**, 1781 (2005).

[99] W. D. Cornell *et al.*, J. Am. Chem. Soc. **117**, 5179 (1995).

[100] G. Chopra and M. Levitt, Proc. Natl. Acad. Sci. (2011).

[101] P. Gallo, M. Rovere, and E. Spohr, Phys. Rev. Lett. **85**, 4317 (2000).

[102] K. Binder, Rep. Prog. Phys. **50**, 783 (1987).

[103] H. E. Stanley, *Introduction to phase transitions and critical phenomena* (Oxford University Press, New York, 1987).

[104] D. V. Matyushov and B. M. Ladanyi, J. Chem. Phys. **110**, 994 (1999).

[105] J. A. D. MacKerrell *et al.*, J. Phys. Chem. B **102**, 3586 (1998).

[106] S. Kumar, K. Bouzida, R. Swendsen, P. Kollman, and J. Rosenberg, J. Comp. Chem. **13**, 1012 (1992).

[107] D. W. Small, D. V. Matyushov, and G. A. Voth, J. Am. Chem. Soc. **125**, 7470 (2003).

[108] J. J. Zhu, R. Ma, Y. Lu, and G. Stell, J. Chem. Phys. **123**, 224505 (2005).

[109] P. Auffinger, T. E. Cheatham III, and A. C. Vaiana, J. Chem. Theory Comput. **3**, 1851 (2007).

[110] I. S. Joung and T. E. Cheatham III, J. Phys. Chem. B **112**, 9020 (2008).

[111] A. D. Friesen and D. V. Matyushov, J. Chem. Phys. **135**, 104501 (2011).

[112] H. J. C. Berendsen, J. P. M. Postma, W. van Bunsteren, A. DiNola, and J. R. Haak, J. Chem. Phys. **81**, 3684 (1984).

[113] T. Morishita, J. Chem. Phys. **113**, 2976 (2000).

[114] P. H. Hünenberger, Thermostat algorithms for molecular dynamics simulations, in *Advanced Computer Simulation*, edited by C. Dr. Holm and K. Prof. Dr. Kremer, , Advances in Polymer Science Vol. 173, pp. 105–149, Springer Berlin / Heidelberg, 2005.

[115] A. Glattli, X. Duara, and W. F. van Gunsteren, J. Chem. Phys. **116**, 9811 (2002).

Appendix A

SIMULATION PROTOCOL FOR NON-POLAR KIHARA CAVITIES

Simulations were performed using the DLPOLY 2.0 molecular dynamics package. Following 100 to 500 ps equilibration, data were collected for 5 ns, with configurations saved every 50 ps. Simulations were performed at 273 K and zero pressure with a timestep of 2 fs. Configurations were saved every 50 timesteps. To allow sufficient hydration layers, the number of waters was changed as the solute size was increased. Table A.1 shows the number of waters used for the different solute sizes. The temperature and pressure were maintained using the Berendsen thermostat and barostat with time constants 0.5 and 0.2 ps, respectively [112]. Cubic boundary conditions were used and the electrostatics were handled by Ewald summation.

Table A.1. Number of hydration waters used in simulations of non-polar Kihara cavities.

r_{0s} (Å)	N
3	4053
3.75	4053
4.5	4048
5.25	5346
6.00	5346
6.75	8871
7.5	5306
8.25	9699
9.00	5887
10.5	8750
12.0	11845

It should be noted that the Berendsen thermostat used here is known not to produce a canonical ensemble[113]. The "weakly coupled" ensemble

actually is somewhere in between the microcanonical and canonical ensembles [113, 114]. We have checked for a few representative points that no significant changes to the results were produced in simulations at constant energy. The dependence of the results on system size was also checked. Our system sizes are in the range where the finite size effect on the reported quantities is negligible. Nevertheless, one must be aware that in general fluctuations can depend on the ensemble used, and we have not strictly checked against a true canonical ensemble. However, it is encouraging to note that our results for the bulk dielectric constant are close to those reported in existing literature[115], and that the results for the chemical potential tend to the expected limit for large cavities.

Appendix B

SIMULATION PROTOCOL FOR KIHARA CAVITY WITH DIPOLE

Nanoscale solutes in water were modeled by the insertion spherical particles in SPC/E water. The solutes consist of a hard-sphere (HS) core, surrounded by a Lennard-Jones (LJ) layer. The interactions of this solute with SPC/E water oxygen are given by a potential of the Kihara type:

$$\phi_{0s}(r) = 4\epsilon_{0s}\left[\left(\frac{\sigma_{0s}}{r - r_{HS}}\right)^{12} - \left(\frac{\sigma_{0s}}{r - r_{HS}}\right)^{6}\right]. \tag{B.1}$$

In the present study, the values of of the parameters were: $r_{HS} = 9$ Å, $\sigma_{0s} = 3$ Å, and $\epsilon_{0s} = 0.65$ kJ/mol. A point dipole was placed at the distance, r_d from the solute center. The dipole was oriented along the radial direction, with the positive end of the dipole toward the interface. The distance from the dipole to the interface is indicated by r_{ds}. We studied solutes with $r_d = 9$ Å and $r_d = 10$ Å. The dipole magnitude, m_0 was varied between 0 and 10 Debye. Simulations were performed at 273 K and 1 atm with 11845 hydration waters. The temperature and pressure were maintained using the Berendsen thermostat and barostat [112]. Most trajectories were 1 ns long following equilibration, although representative points were simulated to 5 ns to check for convergence. Note that the use of the Berendsen thermostat does not produce kinetic energy fluctuations consistent with the canonical ensemble[113]. We expect that the effect on the present results is minimal (see Appendix A for details), but we have not proven this rigorously.

Appendix C

THREE-STATE PHENOMENOLOGICAL MODEL

We introduce a model in which the free energy of fluctuations of the reaction field, R, are given by the superposition of three states, g, 1, 2:

$$e^{-\beta\mathcal{F}(m_0,R)} = e^{-\beta\mathcal{F}_g(m_0,R)} + e^{-\beta\mathcal{F}_1(m_0,R)} + e^{-\beta\mathcal{F}_2(m_0,R)}, \tag{C.1}$$

where:

$$\begin{aligned}
\mathcal{F}_g(m_0,R) =& R^2/(2\kappa_g) - m_0 R \\
\mathcal{F}_1(m_0,R) =& -m_0 R + (R-R_1)^2/(2\kappa_1) + F_1 \\
\mathcal{F}_2(m_0,R) =& -m_0 R + (R-R_2)^2/(2\kappa_2) + F_2,
\end{aligned} \tag{C.2}$$

where $\kappa_{g,1,2}$ are the response functions of the solvent. $F_{1,2}$ is the free energy cost for reaching the excited state and $R_{1,2}$ is the spontaneous reaction field in the excited state.

The average field and variance are found by the usual means:

$$\langle R^n \rangle = Q^{-1} \int \mathrm{d}R \; R^n \; e^{-\beta\mathcal{F}(R)} \tag{C.3}$$

where $Q = \int \mathrm{d}R \; e^{-\beta\mathcal{F}(R)}$. We get for the average:

$$\langle R \rangle = n_g \kappa_g m_0 + n_1(\kappa_1 m_0 + R_1) + n_2(\kappa_2 m_0 + R_2), \tag{C.4}$$

and for the variance:

$$\begin{aligned}
\langle (\delta R)^2 \rangle =& kT(n_g\kappa_g + n_1\kappa_1 + n_2\kappa_2) \\
&+ n_1 n_g \left(m_0(\kappa_1 - \kappa_g) + R_1\right)^2 + n_2 n_g \left(m_0(\kappa_2 - \kappa_g) + R_2\right)^2 \\
&+ n_1 n_2 \left(m_0(\kappa_2 - \kappa_1) + R_2 - R_1\right)^2 .
\end{aligned} \tag{C.5}$$

In [Eq. (C.4)] and [Eq. (C.5)], n_g, n_1 and n_2 are the fractional populations of the three states:

$$\begin{aligned}
n_g^{-1} =& 1 + \sqrt{\frac{\kappa_1}{\kappa_g}} e^{\beta[m_0^2(\kappa_1-\kappa_g)/2 + m_0 R_1 - F_1]} + \sqrt{\frac{\kappa_2}{\kappa_g}} e^{\beta[m_0^2(\kappa_2-\kappa_g)/2 + m_0 R_2 - F_2]} \\
n_1^{-1} =& 1 + \sqrt{\frac{\kappa_2}{\kappa_1}} e^{\beta[m_0^2(\kappa_2-\kappa_1)/2 + m_0(R_2-R_1) + F_1 - F_2]} + \sqrt{\frac{\kappa_g}{\kappa_1}} e^{\beta[m_0^2(\kappa_g-\kappa_1)/2 - m_0 R_1) + F_1]} \\
n_2^{-1} =& 1 + \sqrt{\frac{\kappa_1}{\kappa_2}} e^{\beta[m_0^2(\kappa_1-\kappa_2)/2 + m_0(R_1-R_2) + F_2 - F_1]} + \sqrt{\frac{\kappa_g}{\kappa_2}} e^{\beta[m_0^2(\kappa_g-\kappa_2)/2 - m_0 R_2) + F_2]}.
\end{aligned} \tag{C.6}$$

Appendix D

BOUNDARY VALUE PROBLEM FOR AN OFF-CENTER DIPOLE INSIDE A SPHERICAL CAVITY IN A DIELECTRIC

To find the dielectric response to a dipole off-center, we begin by calculating the potential due to a point charge, q at an arbitrary point inside a sphere with dielectric constant, ϵ_1, immersed in a material with dielectric constant, ϵ_2. The radius of the sphere is r_{0s}, and the location of the charge is $\mathbf{s}$. The potential at the point, $\mathbf{r}$ must satisfy the Poisson equation:

$$\begin{aligned} \epsilon_1 \Delta\phi_1 &= -4\pi\rho \\ \epsilon_2 \Delta\phi_2 &= -4\pi\rho, \end{aligned} \tag{D.1}$$

where ϕ_1 is the potential inside the sphere, and ϕ_2 is the potential outside the sphere. The solution has the following form:

$$\phi = \phi^0 + \phi^{\mathrm{R}} = \frac{1}{\epsilon_1}\frac{1}{|\mathbf{r}-\mathbf{s}|} + \phi^{\mathrm{R}}, \tag{D.2}$$

where ϕ^0 is the simple Coulomb interaction with the point charge and ϕ^{R} is the reaction potential from the surrounding dielectric. Expanding in the Legendre polynomials,

$$\begin{aligned} \phi_1^R &= \sum_{l=0}^{\infty} A_l r^l P_l(\cos\theta) \\ \phi_2^R &= \sum_{l=0}^{\infty} \frac{B_l}{r^{l+1}} P_l(\cos\theta) \\ \phi^0 &= \begin{cases} \sum_{l=0}^{\infty} \frac{1}{\epsilon_1 r}\left(\frac{r}{s}\right)^{l+1} P_l(\cos\theta), & s > r \\ \sum_{l=0}^{\infty} \frac{1}{\epsilon_1 r}\left(\frac{s}{r}\right)^{l+1} P_l(\cos\theta), & r > s \end{cases} \end{aligned} \tag{D.3}$$

The boundary conditions are:

$$\phi_1(r_{0s}) = \phi_2(r_{0s}), \tag{D.4}$$

and:

$$\epsilon_1 \left.\frac{\partial\phi_1}{\partial r}\right|_{r=r_{0s}} = \epsilon_2 \left.\frac{\partial\phi_2}{\partial r}\right|_{r=r_{0s}}. \tag{D.5}$$

Respectively, these require :

$$A_l(r_{0s})^l = B_l/(r_{0s})^{l+1}, \tag{D.6}$$

and:

$$\epsilon_1 l A_l(r_{0s})^{l-1} - \frac{(l+1)s^l}{(r_{0s})^{l+2}} = -\frac{\epsilon_2}{\epsilon_1}\frac{(l+1)s^l}{(r_{0s})^{l+2}} - \frac{\epsilon_2(l+1)B_l}{(r_{0s})^{l+2}}. \tag{D.7}$$

The reaction potential inside the sphere is (dropping the subscript):

$$\phi = -q\frac{\epsilon-1}{r_{0s}}\sum_{l=0}^{\infty} G_l \left(\frac{rs}{(r_{0s})^2}\right)^l P_l(\cos\theta), \tag{D.8}$$

where $\epsilon = \epsilon_2/\epsilon_1$, and:

$$G_l = \frac{l+1}{l\,(\epsilon+1)+\epsilon}. \tag{D.9}$$

The reaction field from a collection of charges q_i at points $\mathbf{s}_i$ is found from the gradient of the reaction potential:

$$\begin{aligned} R_0 =& -\nabla_r \phi^{\mathrm{R}} \\ =& \frac{\epsilon-1}{r\,r_{0s}}\sum_i q_i \sum_{l=0}^{\infty} G_l \left(\frac{r\,s_i}{(r_{0s})^2}\right)^l \left[lP_l(\cos\theta)\hat{\mathbf{r}} - P_l^{'}(\cos\theta)\left(\hat{\mathbf{s}} - \hat{\mathbf{r}}(\hat{\mathbf{s}}\cdot\hat{\mathbf{r}})\right)\right]. \end{aligned} \tag{D.10}$$

The first term in the square brackets is the longitudinal (radial) projection, and the second term is the transverse projection. For a dipole along the radial unit vector ($\cos\theta = 1$), we have two charges, q_1 and q_2, at distances s_1 and $s_2 = s_1 + \Delta s$ from the cavity center. The reaction field is:

$$\begin{aligned} R_0 =& \frac{\epsilon-1}{r\,r_{0s}}\sum_i q_i \sum_{l=1}^{\infty} l\,G_l \left(\frac{r\,s_i}{(r_{0s})^2}\right)^l \\ =& \frac{\epsilon-1}{(r_{0s})^3}\sum_{l=1}^{\infty} G_l \left(\frac{r}{(r_{0s})^2}\right)^{l-1} q\left(s^l - (s+\Delta s)^l\right), \end{aligned} \tag{D.11}$$

where $q = |q_1| = |q_2|$ and $s = s_1$. In the limit of small Δs:

$$q\left(s^l - (s+\Delta s)^l\right) \approx q\,(\Delta s)\,s^{l-1}\,l = -l\,m_0\,s^{l-1}, \tag{D.12}$$

where $m_0 = q\Delta s$ is the dipole moment. The reaction field due to the point dipole is:

$$R_0 = m_0 \frac{\epsilon - 1}{r_{0s}} \sum_{l=1}^{\infty} l^2\,G_l\,\left(\frac{rs}{(r_{0s})^2}\right)^{l-1}. \tag{D.13}$$

For small r, s, the sum converges quickly, and we have:

$$G_l \approx G_1 = 2/(2\epsilon + 1). \tag{D.14}$$

Thus, letting $r \to s$, in the limit of small s, the reaction field at the dipole is:

$$R_0 = m_0 \frac{2(\epsilon - 1)}{(2\epsilon + 1)(r_{0s})^3} \sum_{l=1}^{\infty} l^2 \left(\frac{s^2}{(r_{0s})^2}\right)^{l-1}. \tag{D.15}$$

Representing $(s/r_{0s})^2 = t$, the summation can be written in terms of the geometric series:

$$\frac{d}{dt}\left(t\,\frac{d}{dt}\sum_{l=0}^{\infty} t^l\right) = \frac{d}{dt}\,\left(t\,\frac{d}{dt}\frac{1}{1-t}\right), \tag{D.16}$$

and we obtain:

$$R_0 = R^{(0)} = m_0 \frac{2(\epsilon - 1)}{(2\epsilon + 1)(r_{0s})^3} \times \frac{1 + z^2}{(1 - z^2)^3}, \tag{D.17}$$

where $z = s/r_{0s}$. For s/r_{0s} close to 1, the series converges slowly, and the factors G_l are given by their limiting value for large l:

$$G_l \approx 1/(\epsilon + 1). \tag{D.18}$$

In this case, we get:

$$R_0 = R^{(1)} = m_0 \frac{\epsilon - 1}{(\epsilon + 1)(r_{0s})^3} \times \frac{1 + z^2}{(1 - z^2)^3}. \tag{D.19}$$

For the more general case, $0 < s < r_{0s}$, we can write:

$$R_0 = R^{(0)} + h(z)\left(R^{(1)} - R^{(0)}\right) \tag{D.20}$$

where $h(z) = \left[R_0 - R^{(0)}\right) / \left(R^{(1)} - R^{(0)}\right]$. $h(z)$ can be expanded in the even powers of z. To a good approximation, $h(z) \approx z^2$; then the reaction field for $0 < s < r_{0s}$ is:

$$R_0 = m_0 \frac{\epsilon - 1}{(2\epsilon + 1)(r_{0s})^3} \times \left(2 - \frac{z^2}{\epsilon + 1}\right) \times \frac{1 + z^2}{(1 - z^2)^3}. \tag{D.21}$$

For the comparison of the simulation results with continuum electrostatics, we have used the value, $r_{0s} = 11.5$ Å, on the basis of the following criteria:

1. The first peak of the solute-oxygen radial distribution function occurs around $r \approx r_{HS} + \sigma_{0s} = 12$ Å, although fluctuations bring water molecules to marginally closer distances, since the interface is soft.

2. As the solvent structure is perturbed by the field from the solute dipole, a new feature in the solute-solvent pair correlation function appears at approximately 11 Å from the cavity center. Taking the midpoint between 11 Å and 12 Å is therefore a reasonable estimate of the continuum radius.

3. The local solvent response was expected to scale approximately with the field from the solute dipole at the interface. We found the proper scaling, $(r_{ds})^{-3}$ was produced when r_{0s} is taken to be 11.5 Å.

We therefore concluded that $r_{0s} \approx 11.5$ Å is a physically sensible value for r_{0s}, although we stress that the difficulty in rigorously determining a value for the continuum radius only reinforces the inadequacy of continuum electrostatics at the molecular level.

Appendix E

SOLID ANGLE

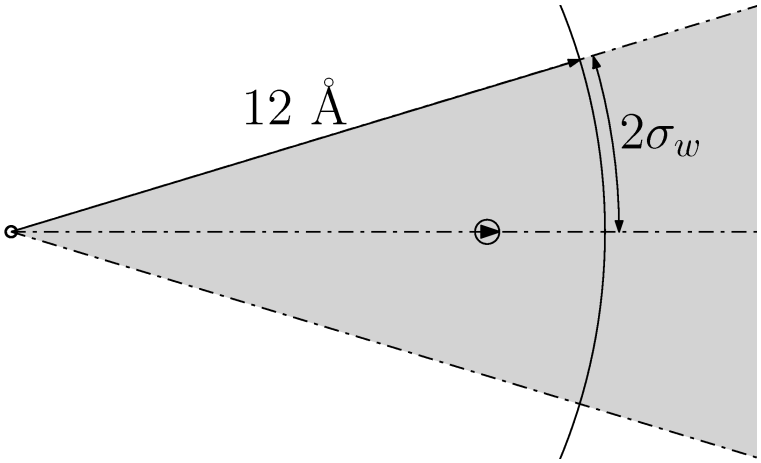

FIG. E.1. Illustration of the solid angle inside which the distributions were calculated. The distance 12 Å is the approximate location of the first peak of the pair correlation function. The solid angle includes all first shell waters within an arc length of $2\sigma_s$ of the dipole axis. The shaded area corresponds to the volume within which the distributions were calculated.

The radial distribution functions and the first shell hydrogen bond angle distributions were calculated for waters inside the solid angle defined as shown in figure E.1. The angle includes the waters within a $2\sigma_s$ (σ_s is the water diameter) arc drawn at a distance of 12 Å from the solute center, at the approximate position of the first maximum in the solute- solvent pair correlation function.

Appendix F

DIPOLAR RESPONSE OF A SUBVOLUME

Here we derive the expression for the dipolar susceptibility of a subvolume to a uniform applied electric field. For simplicity, we take the field $\mathbf{E}_0$ to be along the z direction: $E_0 = \mathbf{E}_0 \cdot \hat{\mathbf{z}} = |\mathbf{E}_0|$. We then focus on the statistics of $M = \mathbf{M} \cdot \hat{\mathbf{z}}$. The dipole moment of the sample in the absence of an applied field will fluctuate with the probability distribution:

$$p_0(M) \propto \int d\Gamma \; e^{-\beta H_0(\Gamma)} \delta(M(\Gamma) - M). \tag{F.1}$$

Where $H_0(\Gamma)$ is the total system Hamiltonian in the absence of an applied field, at the point Γ in phase space. When a field is applied, the energy is modified to:

$$H(\Gamma, E_0) = -ME_0 + H_0(\Gamma). \tag{F.2}$$

Because we are interested in a subvolume, we set $M = M_\Omega + M_2$, where M_Ω is the dipole moment in the subvolume under consideration and M_2 is the dipole of the rest of the sample. We can then calculate the thermodynamic average of M_Ω:

$$\langle M_\Omega \rangle = Q^{-1} \int d\Gamma \; e^{\beta M E_0 - \beta H_0(\Gamma)} M_\Omega, \tag{F.3}$$

where

$$Q = \int d\Gamma \; e^{\beta M E_0 - \beta H_0(\Gamma)} \tag{F.4}$$

is the canonical partition function. The susceptibility can then be found by differentiation:

$$\begin{aligned}
\chi_\Omega &= \Omega^{-1}\frac{\partial\langle M\rangle}{\partial E_0} \\
&= \Omega^{-1}Q^{-1}\int d\Gamma\ \beta e^{-\beta H(\Gamma,E_0)}M_\Omega M - \\
&\quad - Q^{-2}\left(\int d\Gamma\ \beta e^{-\beta H(\Gamma,E_0)}M\right)\times\left(\int d\Gamma\ e^{-\beta H(\Gamma,E_0)}M_\Omega\right) \\
&= \frac{\beta}{\Omega}\left(\langle M_\Omega M\rangle - \langle M_\Omega\rangle\langle M\rangle\right) \\
&= \frac{\beta}{\Omega}\langle\delta M_\Omega\delta M\rangle. \qquad \text{(F.5)}
\end{aligned}$$

The fluctuations of the field are symmetric under rotation, so that $\langle\delta M_\Omega\delta M\rangle = \langle\delta\mathbf{M}_\Omega\cdot\delta\mathbf{M}\rangle/3$, and we get

$$\chi_\Omega = \frac{\beta}{3\Omega}\langle\delta\mathbf{M}_\Omega\cdot\delta\mathbf{M}\rangle. \qquad \text{(F.6)}$$

Appendix G

SIMULATION PROTOCOL FOR FULLERENE

The solute with the geometry of C_{180} was simulated using the NAMD 2 package[98] with 37924 hydration waters. The fullerene was modeled as a rigid solute, with atoms of the type CA from the AMBER force field.[99] Water was represented with the SPC/E model.[75] The temperature was maintained at 310 Kelvin using a Langevin thermostat. Simulations were performed with cubic periodic boundary conditions, and electrostatics were handled by particle mesh Ewald. The system was hydrated in 37924 waters and each system was equilibrated for 5 to 10 ns, before 40 ns production runs. The dipoles on the carbon atoms were represented by two point charges separated by the distance 0.2 Å. At the closest water approach, this makes a difference in the field of less than $\sim 0.3\%$, compared with a true point dipole, and allows the use of the standard integration routines in NAMD.

Appendix H

SIMULATION PROTOCOL FOR CYTOCHROME B562

The protein data bank (PDB) structure 256B was used to build Cytochrome B562 for simulation. The CHARMM all atom force field was used, and the system was hydrated in 33268 TIP3P water molecules. Ions were added to neutralize the system at an ion concentration of 0.1 M. For each umbrella sampling point, the extra charge δq was added to the HEME iron. The balancing charge $-\delta q$ was added to a sodium ion, so that the charge on the sodium ion ranged between -0.6 and 1.6. At each umbrella sampling point, the system was first equilibrated in the NPT ensemble at 1 atm, for 1 ns, then in the NVT ensemble for 7 ns, with a 2 fs timestep. Following equilibration, production runs were 13 ns trajectories in the NVT ensemble at 310 K, with the temperature maintained using a Langevin thermostat. Cubic periodic boundary conditions were used, and the electrostatics were handled by particle mesh Ewald.